

Physical Modeling of Piano Sound

Haifan Xie*

September 24, 2024

Abstract

This paper aims to develop a comprehensive physical model and numerical simulation schemes for a grand piano. The model encompasses various subsystems, including hammer felt, hammer shank, string, soundboard, air and room barriers, each modeled in three dimensions to approach their realistic dynamics. A general framework for 3D elastic solids accounting for prestress and prestrain is introduced, particularly addressing the non-linearities arising from the large deformation of piano strings and the one-sided nature of hammer felt-string contact. The study also examines coupling between subsystem through mechanisms of surface force transmission and displacement/velocity continuity. To facilitate numerical simulations, strong PDEs are translated into weak ODEs via a flexible space discretization approach. Modal transformation of system ODEs is then employed to decouple and reduce DOFs, and an explicit time discretization scheme is customized for generating digital audio in the time domain. The study concludes with a discussion of the piano model's capabilities, limitations, and potential future enhancements.

Contents

1	Introduction	2
2	Preliminary: 3D linear elastic solid with prestress	3
2.1	Strong form (PDEs)	3
2.2	Weak form (ODEs)	5
3	Model for piano soundboard	7
4	Model for piano strings	8
5	Model for sound radiation in the air	9
5.1	Model for the air	9
5.2	Model for the room	12
6	Model for coupling between different parts of the piano	13
6.1	Model for hammer-string coupling	13
6.1.1	One hammer striking one string	13
6.1.2	One hammer striking two or three strings	15
6.2	Model for string-soundboard coupling	17
6.2.1	Static coupling	18
6.2.2	Dynamic coupling	18
6.2.3	More discussions on coupling	19
6.3	Model for soundboard-air and room-air coupling	20
7	Numeric schemes	20
7.1	Modal superposition method for solving coupled ODEs	20
7.1.1	Modal transformation of second-order ODEs	20
7.1.2	Modal transformation of first-order ODEs	22
7.2	Explicit time discretization for coupling between systems	23
7.2.1	Time stepping of second-order ODEs	24
7.2.2	Time stepping of first-order ODEs	25

*Third-year master student, School of Accounting, Guangdong University of Foreign Studies, Guangzhou, China. Email: fan455@outlook.com.

7.2.3	Time stepping of hammer shank rotation ODE	25
7.3	Concatenating the whole model	26
7.3.1	Space discretization	26
7.3.2	Time discretization	26
8	Conclusion	29
A	Prestrain and prestress	32
B	Lagrangian formulation	34
C	Elastic material contacting rigid surface in 3D setting	35
D	An energy-stable scheme for nonlinear forces	37

1 Introduction

This study aims to present a detailed physical model of a grand piano and its numeric implementation schemes. The main features of our model and numeric schemes include:

- As 3D as possible. Subsystems including hammer felt, hammer shank, soundboard, air and room barriers are all fully 3D geometrically modeled. This also means unless for rigid bodies (hammer shank), their 3-directional displacements fully vary with their 3D positions. Our geometric model of piano strings is semi-3D, viz. a cylinder geometry described by coordinates of one axis, but accounts for the strings' 3-directional displacements.
- A general framework for 3D elastic solid, from both Newtonian and Lagrangian perspectives. Rooted in the 3D elasticity theory, this framework not only follows the classic stress-strain relationship, but also introduces a simple and intuitive model for prestrain and prestress. For significantly prestressed structures like piano strings, we offer a more “naturally linear” prestress model compared with the elaborated geometrically exact nonlinear stiff string model in [26]. For nonlinearity due to large deformation, we present a time discretization scheme based on the scalar auxiliary variable (SAV) method [29]. For nonlinearity due to collision, we present a time discretization scheme based on the master-slave approach.
- Consideration of coupling between subsystems of the piano. Two mechanisms are considered here: surface force transmission and displacement/velocity continuity. Furthermore, nonlinear coupling due to collision rather than fixation is considered in the interaction between hammer felt and string, and discussed (but failed to implement) in the interaction between string and two bridge pins.
- A straightforward framework for weak forms and system ordinary differential equations (ODE). For the sake of numeric simulation via the finite element method (FEM), we transform the strong form partial differential equations (PDE) into first or second order system ODEs for each subsystem of the piano. This is achieved via a flexible space discretization framework, which can easily incorporate Dirichlet boundary conditions.
- Modal transformation for solving system ODEs. By solving generalized eigenvalue problems of the mass and stiffness matrices, we decouple the coupled system ODEs and significantly reduce the large vector of degrees of freedom (DOF) into a much smaller vector of modal DOFs.
- An explicit time discretization scheme customized for solving modal ODEs exhibiting source term coupling. This scheme is relatively efficient in that no mid steps are evaluated and no inversion of large non-diagonal matrices is needed. This scheme is relatively accurate in that the rhs source terms of the next time step are used for approximate integration whenever possible, and more than one iteration of numeric integration at each time step may be run to improve convergence.

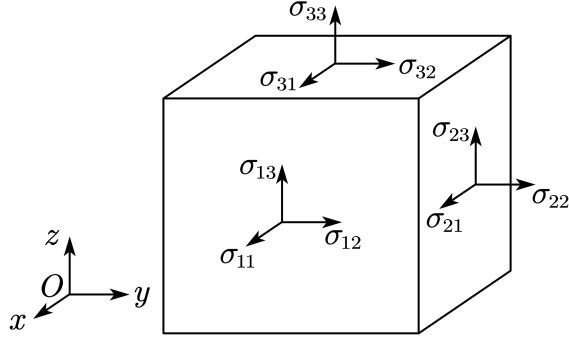


Figure 1: The 9 surface forces acting on the 3 positive sides of an infinitesimal volume

The rest of this paper starts from a basic 3D elastic prestressed solid model in section 2, which will be applied in several cases later. Subsequently sections 3 to 5 introduce models for subsystems of the piano: soundboard, string, air and room barriers. Section 6 investigates the mechanisms for coupling between these subsystems, where hammer felt and shank models are introduced. Section 7 presents the modal superposition method and explicit time stepping schemes to solve the derived system ODEs numerically, and a comprehensive computation procedure for running the simulation. Section 8 gives a brief summary of the whole model and discusses current limitations and future outlooks.

Here we explain some notation patterns that will appear throughout this paper. If not explicitly specified, symbols defined only apply to the current section. In cases where avoiding symbol conflict is necessary, superscripts ^(a), ^(b), ^(c), ^(d), ^(e), ^(f) refer to the string, soundboard, air, hammer shank, hammer felt parts, room barriers of a piano physical system respectively. For the convenience of notation, (x, y, z) and (x_1, x_2, x_3) , (u, v, w) and (u_1, u_2, u_3) are used interchangeably. Bold letters represent vectors or matrices while non-bold letters represent scalars. Definitions for scalars, vectors and matrices with subscript ₀, if not explicitly stated, are automatically inferred from their counterparts without subscript ₀.

2 Preliminary: 3D linear elastic solid with prestress

2.1 Strong form (PDEs)

In this study, the physical models of piano strings and soundboard are based on the full or reduced versions of the linear theory of elasticity [1]. In a 3D Cartesian coordinate system (x, y, z) , consider a material defined over a space $\Omega \subset \mathbb{R}^3$ with a boundary $\Gamma \subset \mathbb{R}^3$, with homogenous or heterogenous density $\rho(x, y, z)$, and dynamic displacements in the 3 directions as

$$\mathbf{u}(x, y, z, t) = [u(x, y, z, t), v(x, y, z, t), w(x, y, z, t)]^\top. \quad (2.1)$$

Based on the displacement field, we shall perform a force analysis of the material, considering two kinds of forces: surface force and body force.

Stress is a major source of surface force for elastic material, and can be derived from the stress-strain relation. The strain matrix (second-order symmetric tensor) is expressed by the gradients of displacements as

$$\boldsymbol{\epsilon} = \begin{bmatrix} \epsilon_{11} & \epsilon_{12} & \epsilon_{13} \\ \epsilon_{12} & \epsilon_{22} & \epsilon_{23} \\ \epsilon_{13} & \epsilon_{23} & \epsilon_{33} \end{bmatrix} = \begin{bmatrix} \partial_x u & \frac{1}{2}(\partial_y u + \partial_x v) & \frac{1}{2}(\partial_z u + \partial_x w) \\ \frac{1}{2}(\partial_y u + \partial_x v) & \partial_y v & \frac{1}{2}(\partial_z v + \partial_y w) \\ \frac{1}{2}(\partial_z u + \partial_x w) & \frac{1}{2}(\partial_z v + \partial_y w) & \partial_z w \end{bmatrix}, \quad (2.2)$$

which is the linearized Green-Lagrange strain. It can also be written in vector form as

$$\vec{\epsilon} = \begin{bmatrix} \epsilon_{11} \\ \epsilon_{22} \\ \epsilon_{33} \\ 2\epsilon_{12} \\ 2\epsilon_{13} \\ 2\epsilon_{23} \end{bmatrix} = \begin{bmatrix} \partial_x u \\ \partial_y v \\ \partial_z w \\ \partial_y u + \partial_x v \\ \partial_z u + \partial_x w \\ \partial_z v + \partial_y w \end{bmatrix} = \sum_{i=1}^3 \mathbf{H}_i \nabla u_i, \quad (2.3)$$

where

$$\mathbf{H}_1 = \begin{bmatrix} 1 & 0 & 0 \\ 0 & 0 & 0 \\ 0 & 0 & 0 \\ 0 & 1 & 0 \\ 0 & 0 & 1 \\ 0 & 0 & 0 \end{bmatrix}, \quad \mathbf{H}_2 = \begin{bmatrix} 0 & 0 & 0 \\ 0 & 1 & 0 \\ 0 & 0 & 0 \\ 1 & 0 & 0 \\ 0 & 0 & 0 \\ 0 & 0 & 1 \end{bmatrix}, \quad \mathbf{H}_3 = \begin{bmatrix} 0 & 0 & 0 \\ 0 & 0 & 0 \\ 0 & 0 & 1 \\ 0 & 0 & 0 \\ 1 & 0 & 0 \\ 0 & 1 & 0 \end{bmatrix}. \quad (2.4)$$

From the generalized Hooke's law, the stress-strain relationship is (here the stress is Cauchy stress)

$$\vec{\sigma} = \begin{bmatrix} \sigma_{11} \\ \sigma_{22} \\ \sigma_{33} \\ \sigma_{12} \\ \sigma_{13} \\ \sigma_{23} \end{bmatrix} = \mathbf{D} \vec{\epsilon}, \quad \mathbf{D} = \begin{bmatrix} D_{11} & D_{12} & D_{13} & D_{14} & D_{15} & D_{16} \\ & D_{22} & D_{23} & D_{24} & D_{25} & D_{26} \\ & & D_{33} & D_{34} & D_{35} & D_{36} \\ & & & D_{44} & D_{45} & D_{46} \\ & & & & D_{55} & D_{56} \\ \text{Sym.} & & & & & D_{66} \end{bmatrix}, \quad (2.5)$$

and the stress matrix (second-order symmetric tensor) is defined as

$$\boldsymbol{\sigma} = \begin{bmatrix} \sigma_{11} & \sigma_{12} & \sigma_{13} \\ \sigma_{12} & \sigma_{22} & \sigma_{23} \\ \sigma_{13} & \sigma_{23} & \sigma_{33} \end{bmatrix}. \quad (2.6)$$

As shown in figure 1, there are 9 stress forces acting on the 3 positive surfaces (as well as 9 stress forces on the 3 negative surfaces not shown) of an infinitesimal volume of material. \mathbf{D} is called the constitutive matrix and its inverse \mathbf{D}^{-1} is called the compliance matrix. The i th row or column of the stress matrix can be expressed as

$$\boldsymbol{\sigma}_i = \sum_{j=1}^3 \mathbf{A}_{ij} \nabla u_j, \quad \mathbf{A}_{ij} = \mathbf{H}_i^\top \mathbf{D} \mathbf{H}_j, \quad \mathbf{A} = \begin{bmatrix} \mathbf{A}_1 \\ \mathbf{A}_2 \\ \mathbf{A}_3 \end{bmatrix} = \begin{bmatrix} \mathbf{A}_{11} & \mathbf{A}_{12} & \mathbf{A}_{13} \\ \mathbf{A}_{21} & \mathbf{A}_{22} & \mathbf{A}_{23} \\ \mathbf{A}_{31} & \mathbf{A}_{32} & \mathbf{A}_{33} \end{bmatrix}, \quad (2.7)$$

where block matrix \mathbf{A} is symmetric. As $\boldsymbol{\sigma}_i$ represents surface forces, converting it to body force would result in $\nabla \cdot \boldsymbol{\sigma}_i$.

Prestress is considered as the initial stress of material in static equilibrium, which is not included in the above analysis of stress. Incorporating prestress into our analysis would require some additional work as presented in appendix A, which we shall refer to. Define the static tension field matrix (second-order symmetric tensor) and its vector form as

$$\mathbf{T}(x, y, z) = \begin{bmatrix} T_{11} & T_{12} & T_{13} \\ T_{12} & T_{22} & T_{23} \\ T_{13} & T_{23} & T_{33} \end{bmatrix}, \quad \vec{\mathbf{T}}(x, y, z) = \begin{bmatrix} T_{11} \\ T_{22} \\ T_{23} \\ T_{12} \\ T_{13} \\ T_{23} \end{bmatrix}, \quad (2.8)$$

which can be visualized by figure 1 similar to stress. Since \mathbf{T} is the prestress in static equilibrium, $\nabla \cdot \mathbf{T} = \mathbf{0}$ should hold (ignoring gravity). As per (A.7), the contribution of prestress to the total stress consists of the static prestress \mathbf{T} , and the dynamic prestress $\boldsymbol{\tau}$ which is also a symmetric tensor. Denote \mathbf{T}_i and $\boldsymbol{\tau}_i$ as the i th row or column of \mathbf{T} and $\boldsymbol{\tau}$ respectively, then we find

$$\boldsymbol{\tau}_i = \sum_{j=1}^3 \mathbf{B}_{ij} \nabla u_j, \quad \mathbf{B}_{ij} = \Psi_0 \mathbf{H}_i^\top \Psi_1^\top \Psi_2^\top \mathbf{D} \Psi_2 \Psi_1 \mathbf{H}_j, \quad \mathbf{B} = \begin{bmatrix} \mathbf{B}_1 \\ \mathbf{B}_2 \\ \mathbf{B}_3 \end{bmatrix} = \begin{bmatrix} \mathbf{B}_{11} & \mathbf{B}_{12} & \mathbf{B}_{13} \\ \mathbf{B}_{21} & \mathbf{B}_{22} & \mathbf{B}_{23} \\ \mathbf{B}_{31} & \mathbf{B}_{32} & \mathbf{B}_{33} \end{bmatrix}, \quad (2.9)$$

where block matrix \mathbf{B} is symmetric; the scalar Ψ_0 and symmetric matrices Ψ_1 and Ψ_2 , all constant w.r.t. unknowns, are defined in appendix A. Similar to σ_i previously discussed, \mathbf{T}_i and τ_i contain the 3 sources of prestress in the same i th axis. For static equilibrium, $\nabla \cdot \mathbf{T}_i = 0$ should hold; then in dynamic states, $\nabla \cdot \tau_i$ is the body force of prestress in the i th axis.

Besides stress and prestress which are conservative, non-conservative forces like damping force often exist. For elastic non-metallic solid, viscoelastic damping is often the predominant damping [15]. We hereby adopt a simple viscoelastic model: the viscous damping force is positively proportional to the first-order time derivative of stress and prestress¹. Occurring on surfaces of small volumes, the damping forces can be visualized by figure 1 similar to stress. The vector of damping forces parallel to the x_i axis is defined as

$$\varsigma_i = 2\mu\partial_t(\sigma_i + \tau_i), \quad (2.10)$$

where $2\mu > 0$ is the damping coefficient. Other damping models can also be incorporated into our model, e.g. structural damping that adds imaginary parts to elasticity coefficients [3]². As for non-conservative forces besides damping, we represent them as a single force $\mathbf{F} = [F_1, F_2, F_3]^\top$ and will investigate them for different physical systems later.

Having derived all the relevant forces acting on an infinitesimal volume of solid material, we can invoke Newton's second law to derive 3 PDEs as

$$\rho\partial_{tt}u_i = \nabla \cdot \mathbf{G}_i + F_i, \quad i = 1, 2, 3. \quad (2.11)$$

where vector $\mathbf{G}_i = \sigma_i + \tau_i + \varsigma_i$ is defined as the i th row or column of symmetric tensor \mathbf{G} representing all surface forces except the static prestress. The above equation can also be derived via a Lagrange formulation of the virtual work and the variations of kinetic and potential energy.

2.2 Weak form (ODEs)

We then seek for a weak form of (2.11) via variational formulation. Multiplying an arbitrary test function vector $\psi(x, y, z)$ on both sides of it and integrating over Ω yields

$$\int_{\Omega} \psi \rho \partial_{tt} u_i dV - \int_{\Omega} \psi \nabla \cdot \mathbf{G}_i dV = \int_{\Omega} \psi F_i dV \quad (2.12)$$

$$\int_{\Omega} \psi \rho \partial_{tt} u_i dV + \int_{\Omega} (\nabla \psi) \mathbf{G}_i dV = \int_{\Omega} \psi F_i dV \quad (2.13)$$

where $dV = dx dy dz$ and applying the gradient operator ∇ to a vector results in its Jacobian matrix. In the above formulation, integration by parts is utilized with Neumann boundary condition imposed as

$$\mathbf{G}_i \cdot d\mathbf{\Gamma} = 0, \quad (2.14)$$

where $d\mathbf{\Gamma}$ is the outward normal vector of the tangent plane of any point on Γ . Note that this condition applies only when the test function is non-zero on the boundary, viz. Neumann boundary conditions need not be satisfied at points where Dirichlet boundary conditions are present.

We now use space discretization and the Galerkin method to transform (2.13) into second-order ODE. Based on (2.1), define the displacement field of the soundboard as $\mathbf{u}^* \approx \mathbf{u} = [u, v, w]^\top$ (here superscript * means the exact solution) as

$$\begin{aligned} u(x, y, z, t) &= \varphi_1(x, y, z) \cdot [\mathbf{S}_1 \boldsymbol{\xi}(t) + \mathbf{S}_{0,1} \boldsymbol{\xi}_0(t)], \\ v(x, y, z, t) &= \varphi_2(x, y, z) \cdot [\mathbf{S}_2 \boldsymbol{\xi}(t) + \mathbf{S}_{0,2} \boldsymbol{\xi}_0(t)], \\ w(x, y, z, t) &= \varphi_3(x, y, z) \cdot [\mathbf{S}_3 \boldsymbol{\xi}(t) + \mathbf{S}_{0,3} \boldsymbol{\xi}_0(t)], \end{aligned} \quad (2.15)$$

¹An explanation for this is that stress and prestress, along with viscous damping force, are resistance to deformation, and so their relations should be positive.

²The original real constitutive matrix is symmetric. If we add imaginary values to it, it may be beneficial to make it an Hermitian matrix. This way energy may be dissipated to the imaginary part of the system but not outside the system, i.e. energy is still conserved within the system.

where the sizes of vectors and matrices are

$$\begin{aligned}
&\boldsymbol{\xi} : N \times 1, \boldsymbol{\xi}_0 : N_0 \times 1, \\
&\boldsymbol{\varphi}_1 : N_1 \times 1, \mathbf{S}_1 : N_1 \times N, \mathbf{S}_{0,1} : N_{0,1} \times N_0, \\
&\boldsymbol{\varphi}_2 : N_2 \times 1, \mathbf{S}_2 : N_2 \times N, \mathbf{S}_{0,2} : N_{0,2} \times N_0, \\
&\boldsymbol{\varphi}_3 : N_3 \times 1, \mathbf{S}_3 : N_3 \times N, \mathbf{S}_{0,3} : N_{0,3} \times N_0.
\end{aligned} \tag{2.16}$$

In (2.15), each scalar displacement unknown is expressed as the dot product of a space function vector and time function vector. In FEM, $\boldsymbol{\varphi}_i$ is the vector of shape functions (also known as interpolation functions) for variable u_i , and $\boldsymbol{\vartheta}_i = \mathbf{S}_i \boldsymbol{\xi} + \mathbf{S}_{0,i} \boldsymbol{\xi}_0$ is the vector of coefficients of shape functions, often interpreted as nodal displacements. The only unknown here is $\boldsymbol{\xi}(t)$, the vector of unknown DOFs, whereas other vectors and matrices are known. $\boldsymbol{\xi}(t)$ is defined so that through some linear transformation by \mathbf{S}_1 and $\mathbf{S}_{0,1} \boldsymbol{\xi}_0(t)$, the nodal displacements $\boldsymbol{\vartheta}_i$ can be obtained. The reason we do not simply define $u_i = \boldsymbol{\varphi}_i \cdot \boldsymbol{\xi}_i$ but consider a linear transformation is that it provides additional flexibility when imposing Dirichlet boundary conditions. For instance, when $u + v$ rather than u or v is known to be some nonzero functions on the space boundary, $\boldsymbol{\xi}$ only needs to contain u and $u + v$ is incorporated in $\boldsymbol{\xi}_0$. We can thus see that total DOF, viz. the number of time functions we need to solve, is N that does not necessarily equal to $N_1 + N_2 + N_3$. Often in simple cases, matrix $\mathbf{S} = [\mathbf{S}_1^\top, \mathbf{S}_2^\top, \mathbf{S}_3^\top]^\top$ is diagonal with many ones and some zeros on the diagonal.

To express the displacement and its gradient in the DOF vector, we find the below relations:

$$\begin{aligned}
u_i &= \mathbf{P}_i \boldsymbol{\xi} + \mathbf{P}_{0,i} \boldsymbol{\xi}_0, \mathbf{u} = \mathbf{P} \boldsymbol{\xi} + \mathbf{P}_0 \boldsymbol{\xi}_0, \nabla u_i = \mathbf{Q}_i \boldsymbol{\xi} + \mathbf{Q}_{0,i} \boldsymbol{\xi}_0, \\
\mathbf{P} &= \begin{bmatrix} \mathbf{P}_1 \\ \mathbf{P}_2 \\ \mathbf{P}_3 \end{bmatrix} = \begin{bmatrix} \boldsymbol{\varphi}_1^\top \mathbf{S}_1 \\ \boldsymbol{\varphi}_2^\top \mathbf{S}_2 \\ \boldsymbol{\varphi}_3^\top \mathbf{S}_3 \end{bmatrix}, \mathbf{P}_0 = \begin{bmatrix} \mathbf{P}_{0,1} \\ \mathbf{P}_{0,2} \\ \mathbf{P}_{0,3} \end{bmatrix} = \begin{bmatrix} \boldsymbol{\varphi}_1^\top \mathbf{S}_{0,1} \\ \boldsymbol{\varphi}_2^\top \mathbf{S}_{0,2} \\ \boldsymbol{\varphi}_3^\top \mathbf{S}_{0,3} \end{bmatrix}, \\
\mathbf{Q} &= \begin{bmatrix} \mathbf{Q}_1 \\ \mathbf{Q}_2 \\ \mathbf{Q}_3 \end{bmatrix} = \begin{bmatrix} (\nabla \boldsymbol{\varphi}_1)^\top \mathbf{S}_1 \\ (\nabla \boldsymbol{\varphi}_2)^\top \mathbf{S}_2 \\ (\nabla \boldsymbol{\varphi}_3)^\top \mathbf{S}_3 \end{bmatrix}, \mathbf{Q}_0 = \begin{bmatrix} \mathbf{Q}_{0,1} \\ \mathbf{Q}_{0,2} \\ \mathbf{Q}_{0,3} \end{bmatrix} = \begin{bmatrix} (\nabla \boldsymbol{\varphi}_1)^\top \mathbf{S}_{0,1} \\ (\nabla \boldsymbol{\varphi}_2)^\top \mathbf{S}_{0,2} \\ (\nabla \boldsymbol{\varphi}_3)^\top \mathbf{S}_{0,3} \end{bmatrix}.
\end{aligned} \tag{2.17}$$

Combining (2.17) with (2.7) (2.9), the following relations are found:

$$\begin{aligned}
\boldsymbol{\sigma}_i &= \mathbf{A}_i \mathbf{Q} \boldsymbol{\xi} + \mathbf{A}_i \mathbf{Q}_0 \boldsymbol{\xi}_0, \\
\boldsymbol{\tau}_i &= \mathbf{B}_i \mathbf{Q} \boldsymbol{\xi} + \mathbf{B}_i \mathbf{Q}_0 \boldsymbol{\xi}_0,
\end{aligned} \tag{2.18}$$

Now we substitute (2.17) (2.18) into (2.11) (2.12) (2.13), and use \mathbf{P}_i^\top as a vector of test functions for the i th PDE. These would yield 3 groups of weak-form equations, each group having N equations. Summing the 3 groups into 1 group, we derive a system of N coupled second-order ODEs as

$$\mathbf{M} \ddot{\boldsymbol{\xi}}(t) + \mathbf{C} \dot{\boldsymbol{\xi}}(t) + \mathbf{K} \boldsymbol{\xi}(t) = \mathbf{f}(t), \tag{2.19}$$

where

$$\begin{aligned}
\mathbf{M} &= \int_{\Omega} \rho \mathbf{P}^\top \mathbf{P} dV, \mathbf{M}_0 = \int_{\Omega} \rho \mathbf{P}^\top \mathbf{P}_0 dV, \\
\mathbf{K} &= \int_{\Omega} \mathbf{Q}^\top (\mathbf{A} + \mathbf{B}) \mathbf{Q} dV, \mathbf{K}_0 = \int_{\Omega} \mathbf{Q}^\top (\mathbf{A} + \mathbf{B}) \mathbf{Q}_0 dV, \\
\mathbf{C} &= 2\mu \mathbf{K}, \mathbf{C}_0 = 2\mu \mathbf{K}_0, \\
\mathbf{f}(t) &= \mathbf{f}_0(t) + \mathbf{f}_1(t), \\
\mathbf{f}_0(t) &= -\mathbf{M}_0 \ddot{\boldsymbol{\xi}}_0 - \mathbf{C}_0 \dot{\boldsymbol{\xi}}_0 - \mathbf{K}_0 \boldsymbol{\xi}_0, \mathbf{f}_1(t) = \int_{\Omega} \mathbf{P}^\top \mathbf{F} dV
\end{aligned} \tag{2.20}$$

are called the mass matrix, stiffness matrix, damping matrix and force vector respectively. In the next following sections, we shall apply the above 3D elastic solid material model to various parts of the piano physical system, including soundboard, string, room material and hammer felt.

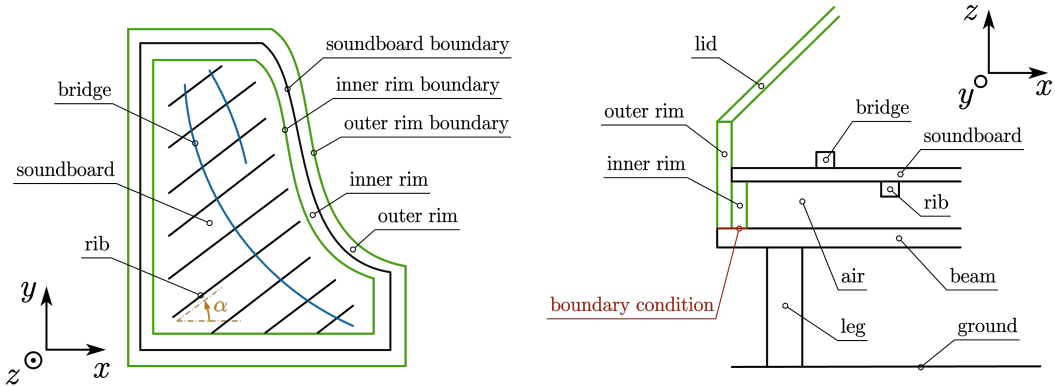


Figure 2: The piano soundboard in top view (left) and side view (right)

3 Model for piano soundboard

The study treats the grand piano soundboard as a multi-layer plate with irregular geometry, and physically models it as a 3D structure. In [10, 11, 13], the soundboard was modeled as a Reissner-Mindlin plate, accounting for the ribs and bridges by making the thickness, density, and elastic coefficients position-dependent; however, it is unclear how the different orthotropic angles of each layer were handled. In [33], the soundboard was modeled as a Kirchhoff-Love plate, considering a 90 degrees orthotropic rotation of the ribs; however, as the Kirchhoff-Love plate specifies only 1 unknown for the 3D displacement field, it may not be accurate enough, especially regarding the ribs and bridges which are much thicker than the board. In [34, 25], the soundboard was modeled as a 3D structure using tetrahedral elements, then reduced it into a modal model; this is an advancement from 2D to 3D soundboard, but the authors have not presented much details regarding the 3D equations. Moreover, some features of the soundboard seem still under-evaluated: the prestress exerted by the string on the soundboard; the role of rim and lid in the soundboard's vibration; the more exact 2D Dirichlet boundary conditions for the 3D soundboard, different from the case of 1D boundary conditions for 2D soundboard.

To better account for the soundboard's multi-layer feature, the current study implements a fully 3D soundboard model. Figure 2 shows a simplified soundboard sketch based on [23]. In our physical model, the soundboard is an entity composed of 5 parts: board, ribs, bridges, rim, lid. The board is parallel to the xOy plane, with the ribs attached to its under side and the bridges attached to its upper side. The horizontal fibers of the board and bridges are approximately parallel, while the horizontal fibers of ribs are almost orthogonal to that of the board. The rim consists of 2 parts: the inner rim connects the board's boundary from below using bolts and dowels, and the outer rim encases the board and the lower rim. The lid, as large as the board and with an angle to it, is an extension of the outer rim through a wooden stick (considered part of the lid) and hinges. All parts of the soundboard are treated as a whole in computation, meaning that the displacements of part intersections are uniform.

The soundboard's governing PDEs follow (2.11) and ODEs follow (2.19), so we do not need to present them again. We only need to discuss some parameters, initial conditions and boundary conditions here. Define the occupied space of soundboard as $\Omega \subset \mathbb{R}^3$, and the boundaries of soundboard as $\Gamma_1, \Gamma_2 \subset \Gamma \subset \mathbb{R}^3$. Here Γ contains all the 2D surfaces of the 3D volume of soundboard; Γ_1 contains only the underside surfaces of the inner and outer rims, as marked red at the right of figure 2; Γ_2 is Γ excluding Γ_1 , the vibrating parts. We shall see in the following that Γ_1 and Γ_2 are where the Dirichlet boundary conditions apply to the soundboard and the air respectively.

Given that all parts of the soundboard are mainly made of wood, an orthotropic material

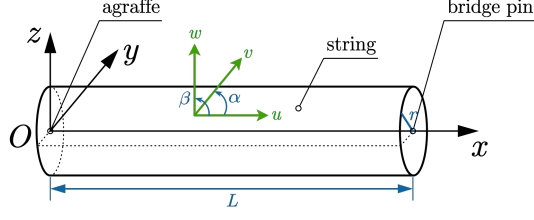


Figure 3: The piano string in 3D view

whose orthotropic directions are determined by fibers [7], the compliance matrix writes

$$\mathbf{D}_{\text{orth}}^{-1} = \begin{bmatrix} \frac{1}{E_x} & -\frac{\nu_{xy}}{E_x} & -\frac{\nu_{xz}}{E_x} & 0 & 0 & 0 \\ & \frac{1}{E_y} & -\frac{\nu_{yz}}{E_y} & 0 & 0 & 0 \\ & & \frac{1}{E_z} & 0 & 0 & 0 \\ & & & G_{xy} & 0 & 0 \\ & & & & G_{xz} & 0 \\ \text{Sym.} & & & & & G_{yz} \end{bmatrix}, \quad (3.1)$$

where E , G , ν are the young's modulus, shear modulus and Poisson's ratio. Note that different layers would have different elastic coefficients. It is then necessary to consider that for a certain layer like ribs, the global axes x, y may need to be rotated by an angle α , as denoted in figure 2, to become the material orthotropic axes x', y' and for a certain layer. The actual constitutive matrix is then

$$\mathbf{D} = \mathbf{Z}^\top \mathbf{D}_{\text{orth}} \mathbf{Z}, \quad \mathbf{Z} = \begin{bmatrix} C^2 & S^2 & 0 & SC & 0 & 0 \\ S^2 & C^2 & 0 & -SC & 0 & 0 \\ 0 & 0 & 1 & 0 & 0 & 0 \\ -2SC & 2SC & 0 & C^2 - S^2 & 0 & 0 \\ 0 & 0 & 0 & 0 & C & S \\ 0 & 0 & 0 & 0 & -S & C \end{bmatrix}, \quad (3.2)$$

where $S = \sin \alpha, C = \cos \alpha$. Readers may refer to [27] for a detailed deduction. After rotation, the constitutive matrix would have 13 non-zero entries for its upper triangular part.

As for initial and boundary conditions, equation (2.11) is constrained by:

$$\mathbf{u}|_{\mathbf{x} \in \Gamma_1} = \mathbf{0}, \quad (3.3)$$

$$\mathbf{u}|_{t=0} = \partial_t \mathbf{u}|_{t=0} = \mathbf{0}. \quad (3.4)$$

The choice of this boundary condition stems from that the whole soundboard is hard supported by beams and legs on the under side of rim (see figure 2). Thanks to the flexibility of our 3D model, the rim can be treated as a natural extension of the main board, thereby capturing more nuanced boundary conditions compared to the clamped or simply supported cases in 2D models. Given appropriate boundary conditions, the mass and stiffness matrices are symmetric positive definite.

4 Model for piano strings

The symbols in this section follow sections 2 and 3 if not explicitly defined. Definitions for scalars, vectors and matrices with subscript $_0$, if not explicitly stated, are automatically inferred from their counterparts without subscript $_0$.

The study treats a grand piano string as a cylinder material, and physically models it as a 1D beam prestressed longitudinally. As shown in figure 3, the string is fixed at the agraffe end (immobile) and coupled to the bridge end (mobile) [9] through pins. Define that the central line of string range start from the tuning pin $[-L_0, 0, 0]^\top$, then go through the agraffe $\mathbf{x}_0 = [0, 0, 0]^\top$, the front bridge pin $\mathbf{x}_1 = [L_1, 0, 0]^\top$, the rear bridge pin $\mathbf{x}_2 = [L_2, 0, 0]^\top$, and finally the hitch pin

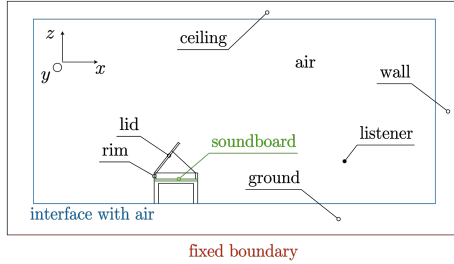


Figure 4: The piano in a room

$\mathbf{x}_3 = [L_3, 0, 0]^\top$, where L_3 is the so-called “speaking length”; let r be the radius of cross-section and ρ be the homogenous density per unit volume. It is known that the vibration of piano strings is primarily vertical (z direction) [4]. Nevertheless, longitudinal vibration (x direction) [5] and horizontal vibration (y direction) [31] may also be essential, as they contribute respectively to the sound precursor [9] and double-decay [32] phenomena. Two more kinds of vibration that require attention are the rotations of the string’s cross-section towards the y and z axes, so as to account for the stiffness of piano strings that may result in slightly inharmonic sounds [10].

To incorporate all these essential kinds of vibrations, define the displacement field of a piano string as $\mathbf{u}^* \approx \mathbf{u} = [u, v, w]^\top$ in a similar notion to (2.15). In addition, we specify that

$$\begin{aligned} \boldsymbol{\varphi}_1(x, y, z) &= \begin{bmatrix} \varphi_{11}(x) \\ -y\varphi_{12}(x) \\ -z\varphi_{13}(x) \end{bmatrix}, \quad \mathbf{S}_1 = \begin{bmatrix} \mathbf{S}_{11} \\ \mathbf{S}_{12} \\ \mathbf{S}_{13} \end{bmatrix}, \\ \boldsymbol{\varphi}_2(x, y, z) &= \boldsymbol{\varphi}_2(x), \quad \boldsymbol{\varphi}_3(x, y, z) = \boldsymbol{\varphi}_3(x), \end{aligned} \quad (4.1)$$

where subscripts $_{11,2,3}, _{12}, _{13}$ refer to vectors or matrices defined for longitudinal, horizontal, vertical, horizontal rotational and vertical rotational vibrations respectively, as marked u, v, w, α, β in figure 3. Definition for $\boldsymbol{\varphi}_{0,1}$ and $\mathbf{S}_{0,1}$ are similar to the above. From a 3D perspective, it can be seen that with regard to the y and z axes, the x displacement is first-order modeled, while the y and z displacements are zeroth-order modeled. As the steel used to manufacture piano strings can be considered as isotropic material, the elasticity coefficients in (3.1) simplifies to

$$\begin{aligned} E &= E_x = E_y = E_z, \\ \nu &= \nu_{xy} = \nu_{xz} = \nu_{yz}, \\ G &= \frac{E}{2(1 + \nu)} = G_{xy} = G_{xz} = G_{yz}. \end{aligned} \quad (4.2)$$

It now suffices to derive a system of N coupled second-order ODEs similar to (2.19) (2.20). In order that reasonable solutions can be found, equation (2.11) is at least constrained by the following Dirichlet boundary conditions:

$$\mathbf{u}|_{x=0} = \mathbf{u}|_{x=L_3} = \mathbf{0}, \quad (4.3)$$

which means the motion of string vanishes at the agraffe point and the hitch point. Another Dirichlet boundary condition at the coupling point \mathbf{x}_1 will be discussed in section 6. The initial conditions are

$$\mathbf{u}|_{t=0} = \partial_t \mathbf{u}|_{t=0} = \mathbf{0}. \quad (4.4)$$

5 Model for sound radiation in the air

5.1 Model for the air

The study adopts a 3D acoustic wave model to simulate piano sound radiation in the air. For simulating wave propagation from the piano soundboard to a listener situated at a particular location, [20] used Rayleigh integral to compute the acoustic pressure field, which is able to simulate the different delays and decays of sound at different positions, but unable to account

for boundary conditions. [10, 11, 13] used 2 first-order linear acoustic equations for 4 coupled unknowns: acoustic pressure (1 unknown) and acoustic velocity (3 unknowns). This approach excels at capturing reflections at spatial boundaries like walls and soundboard-air coupling, but seems unable to produce decaying room impulse response due to the absence of damping terms³.

Fluid dynamics exhibit both linear and nonlinear behaviours as described by the Navier-Stokes equation, but considering that sound pressure fluctuations in air are often small, linearized models for sound radiation in the air can achieve a satisfactory level of accuracy for us. The acoustic radiation equations we utilize are based on the linearized fluid dynamics equations [19], including conservation of mass and momentum. It works for isotropic, compressible, viscous, adiabatic flow with homogenous ambient states, in Eulerian description. Damping due to heat conduction is simplified away here and readers may refer to [21, 22] for incorporating it. The governing PDEs write

$$\frac{1}{\rho c^2} \dot{p} + \nabla \cdot \mathbf{u} = 0, \quad (5.1)$$

$$\rho \dot{\mathbf{u}} = \nabla \cdot \mathbf{G} + \mathbf{F}, \quad (5.2)$$

where $\mathbf{u}(x, y, z, t)$ is the acoustic velocity field; $p(x, y, z, t)$ is the perturbation of acoustic pressure field, also should be the final digital audio signal; ρ is the air density; c is the sound propagation speed in the air; \mathbf{G} is the symmetric surface force tensor; the gradient operator ∇ applied to a vector returns its Jacobian matrix, and the divergence operator $\nabla \cdot$ applied to a matrix returns a vector of each row's divergence; $\mathbf{F} = [F_1, F_2, F_3]^\top$ is the external force (viz. body force) treated as zero in this study. According to the Navier-Stokes equation, the surface force tensor \mathbf{G} is defined as

$$\mathbf{G} = -p\mathbf{I} + \mu_1 (\nabla \mathbf{u} + (\nabla \mathbf{u})^\top) + \mu_2 (\nabla \cdot \mathbf{u})\mathbf{I}, \quad (5.3)$$

where μ_1 and μ_B are dynamic viscosity and bulk viscosity coefficients accounting for energy dissipation, and $\mu_2 = \mu_B - \frac{2}{3}\mu_1$. To express the divergence of surface force using acoustic velocity gradients, we find

$$\nabla \cdot \mathbf{G}_i = -\nabla p + \nabla \cdot \boldsymbol{\varsigma}_i, \quad \boldsymbol{\varsigma}_i = \sum_{j=1}^3 (\mu_1 \mathbf{A}_{ij} + \mu_2 \mathbf{B}_{ij}) \nabla u_j,$$

$$\mathbf{A} = \begin{bmatrix} \mathbf{A}_1 \\ \mathbf{A}_2 \\ \mathbf{A}_3 \end{bmatrix} = \begin{bmatrix} \mathbf{A}_{11} & \mathbf{A}_{12} & \mathbf{A}_{13} \\ \mathbf{A}_{21} & \mathbf{A}_{22} & \mathbf{A}_{23} \\ \mathbf{A}_{31} & \mathbf{A}_{32} & \mathbf{A}_{33} \end{bmatrix}, \quad \mathbf{B} = \begin{bmatrix} \mathbf{B}_1 \\ \mathbf{B}_2 \\ \mathbf{B}_3 \end{bmatrix} = \begin{bmatrix} \mathbf{B}_{11} & \mathbf{B}_{12} & \mathbf{B}_{13} \\ \mathbf{B}_{21} & \mathbf{B}_{22} & \mathbf{B}_{23} \\ \mathbf{B}_{31} & \mathbf{B}_{32} & \mathbf{B}_{33} \end{bmatrix},$$

$$\mathbf{A} = \left[\begin{array}{ccc|ccc|ccc} 2 & 0 & 0 & 0 & 0 & 0 & 0 & 0 & 0 \\ 0 & 1 & 0 & 1 & 0 & 0 & 0 & 0 & 0 \\ 0 & 0 & 1 & 0 & 0 & 0 & 1 & 0 & 0 \\ \hline 0 & 1 & 0 & 1 & 0 & 0 & 0 & 0 & 0 \\ 0 & 0 & 0 & 0 & 2 & 0 & 0 & 0 & 0 \\ 0 & 0 & 0 & 0 & 0 & 1 & 0 & 1 & 0 \\ \hline 0 & 0 & 1 & 0 & 0 & 0 & 1 & 0 & 0 \\ 0 & 0 & 0 & 0 & 0 & 1 & 0 & 1 & 0 \\ 0 & 0 & 0 & 0 & 0 & 0 & 0 & 0 & 2 \end{array} \right], \quad \mathbf{B} = \left[\begin{array}{ccc|ccc|ccc} 1 & 0 & 0 & 0 & 1 & 0 & 0 & 0 & 1 \\ 0 & 0 & 0 & 0 & 0 & 0 & 0 & 0 & 0 \\ 0 & 0 & 0 & 0 & 0 & 0 & 0 & 0 & 0 \\ \hline 0 & 0 & 0 & 0 & 0 & 0 & 0 & 0 & 0 \\ 1 & 0 & 0 & 0 & 1 & 0 & 0 & 0 & 1 \\ 0 & 0 & 0 & 0 & 0 & 0 & 0 & 0 & 0 \\ \hline 0 & 0 & 0 & 0 & 0 & 0 & 0 & 0 & 0 \\ 0 & 0 & 0 & 0 & 0 & 0 & 0 & 0 & 0 \\ 1 & 0 & 0 & 0 & 1 & 0 & 0 & 0 & 1 \end{array} \right], \quad (5.4)$$

where \mathbf{G}_i , $\boldsymbol{\varsigma}_i$ is the i th column or row of \mathbf{G} , $\boldsymbol{\varsigma}$; here $\boldsymbol{\varsigma}$ is the damping force tensor. The 2 PDEs

³It seems the acoustic model in [11] relies on soundboard-air coupling to produce the damping. When the acoustic equations are fully coupled to the soundboard equations, the soundboard's damping mechanisms may apply to the air as well. This means even if the acoustic equations contains no damping, the overall energy may be still stable and waves with infinite amplitudes would not occur. However, we choose to add viscous damping terms to the acoustic equations for two reasons. Firstly, it can be observed in audio recording that a very short impulse in a room gets a decaying response, which attributes to the reverberation effect. Secondly, the coupling computation approach we shall introduce later actually relies on decoupling and iterative strategies, meaning that without the room itself's damping mechanisms the computed pressure may exhibit infinite amplitudes.

(5.1) (5.16) then become⁴

$$\rho \dot{u}_i - \nabla \cdot \boldsymbol{\varsigma}_i + \partial_{x_i} p = F_i \quad (i = 1, 2, 3), \quad (5.5)$$

$$\dot{p} + \rho c^2 \nabla \cdot \mathbf{u} = 0, \quad (5.6)$$

where the divergence of velocity can be expressed in velocity gradients as

$$\nabla \cdot \mathbf{u} = \sum_{j=1}^3 \mathbf{H}_j \nabla u_j, \quad \mathbf{H} = \begin{bmatrix} \mathbf{H}_1 & \mathbf{H}_2 & \mathbf{H}_3 \end{bmatrix} = \left[\begin{array}{ccc|ccc} 1 & 0 & 0 & 0 & 0 & 0 \\ 0 & 0 & 0 & 0 & 1 & 0 \\ 0 & 0 & 0 & 0 & 0 & 0 \\ \hline 0 & 0 & 0 & 0 & 0 & 1 \end{array} \right]. \quad (5.7)$$

For acoustic modes the vorticity $\nabla \times \mathbf{u} = \mathbf{0}$ may be assumed zero so that a decoupled equation containing only p as unknown may be obtained, but we choose to not do so because the velocity field of any solid to couple with may not satisfy zero vorticity.

Now we seek for the weak forms of (5.5) (5.6) via the Galerkin method. Multiplying an arbitrary test function vector $\boldsymbol{\psi}$ on both sides of (5.5) yields

$$\begin{aligned} \int_{\Omega} \boldsymbol{\psi} \rho \dot{u}_i dV - \int_{\Omega} \boldsymbol{\psi} (\nabla \cdot \boldsymbol{\varsigma}_i) dV + \int_{\Omega} \boldsymbol{\psi} \partial_{x_i} p dV &= \int_{\Omega} \boldsymbol{\psi} F_i dV \\ \int_{\Omega} \boldsymbol{\psi} \rho \dot{u}_i dV + \int_{\Omega} (\nabla \boldsymbol{\psi}) \boldsymbol{\varsigma}_i dV + \int_{\Omega} \boldsymbol{\psi} \partial_{x_i} p dV &= \int_{\Omega} \boldsymbol{\psi} F_i dV. \end{aligned} \quad (5.8)$$

When using integration by parts in the above, Neumann boundary condition is imposed as

$$\boldsymbol{\varsigma}_i \cdot d\boldsymbol{\Gamma} = 0, \quad (5.9)$$

where $d\boldsymbol{\Gamma}$ is the outward normal vector of the tangent plane of any point on the boundary of acoustic space. This condition means the damping force should vanish on the non-Dirichlet boundaries. Similarly for (5.6), multiplying a test function vector results in

$$\int_{\Omega} \boldsymbol{\psi} \dot{p} dV + \int_{\Omega} \boldsymbol{\psi} \rho c^2 (\nabla \cdot \mathbf{u}) dV = 0. \quad (5.10)$$

To derive the ODEs, we define space discretization similar to (2.15), but with one more variable p , as

$$\begin{aligned} u(x, y, z, t) &= \boldsymbol{\varphi}_1(x, y, z) \cdot [\mathbf{S}_1 \boldsymbol{\xi}(t) + \mathbf{S}_{0,1} \boldsymbol{\xi}_0(t)], \\ v(x, y, z, t) &= \boldsymbol{\varphi}_2(x, y, z) \cdot [\mathbf{S}_2 \boldsymbol{\xi}(t) + \mathbf{S}_{0,2} \boldsymbol{\xi}_0(t)], \\ w(x, y, z, t) &= \boldsymbol{\varphi}_3(x, y, z) \cdot [\mathbf{S}_3 \boldsymbol{\xi}(t) + \mathbf{S}_{0,3} \boldsymbol{\xi}_0(t)], \\ p(x, y, z, t) &= \boldsymbol{\varphi}_4(x, y, z) \cdot [\mathbf{S}_4 \boldsymbol{\xi}(t) + \mathbf{S}_{0,4} \boldsymbol{\xi}_0(t)]. \end{aligned} \quad (5.11)$$

And similar to (2.17), we define convenience matrices to express that

$$\begin{aligned} \mathbf{u} &= \mathbf{P} \boldsymbol{\xi} + \mathbf{P}_0 \boldsymbol{\xi}_0, \quad u_i = \mathbf{P}_i \boldsymbol{\xi} + \mathbf{P}_{0,i} \boldsymbol{\xi}_0, \quad \nabla u_i = \mathbf{Q}_i \boldsymbol{\xi} + \mathbf{Q}_{0,i} \boldsymbol{\xi}_0, \\ \mathbf{P} &= \begin{bmatrix} \mathbf{P}_1 \\ \mathbf{P}_2 \\ \mathbf{P}_3 \end{bmatrix} = \begin{bmatrix} \boldsymbol{\varphi}_1^\top \mathbf{S}_1 \\ \boldsymbol{\varphi}_2^\top \mathbf{S}_2 \\ \boldsymbol{\varphi}_3^\top \mathbf{S}_3 \end{bmatrix}, \quad \mathbf{P}_0 = \begin{bmatrix} \mathbf{P}_{0,1} \\ \mathbf{P}_{0,2} \\ \mathbf{P}_{0,3} \end{bmatrix} = \begin{bmatrix} \boldsymbol{\varphi}_1^\top \mathbf{S}_{0,1} \\ \boldsymbol{\varphi}_2^\top \mathbf{S}_{0,2} \\ \boldsymbol{\varphi}_3^\top \mathbf{S}_{0,3} \end{bmatrix}, \\ \mathbf{Q} &= \begin{bmatrix} \mathbf{Q}_1 \\ \mathbf{Q}_2 \\ \mathbf{Q}_3 \end{bmatrix} = \begin{bmatrix} (\nabla \boldsymbol{\varphi}_1)^\top \mathbf{S}_1 \\ (\nabla \boldsymbol{\varphi}_2)^\top \mathbf{S}_2 \\ (\nabla \boldsymbol{\varphi}_3)^\top \mathbf{S}_3 \end{bmatrix}, \quad \mathbf{Q}_0 = \begin{bmatrix} \mathbf{Q}_{0,1} \\ \mathbf{Q}_{0,2} \\ \mathbf{Q}_{0,3} \end{bmatrix} = \begin{bmatrix} (\nabla \boldsymbol{\varphi}_1)^\top \mathbf{S}_{0,1} \\ (\nabla \boldsymbol{\varphi}_2)^\top \mathbf{S}_{0,2} \\ (\nabla \boldsymbol{\varphi}_3)^\top \mathbf{S}_{0,3} \end{bmatrix}, \\ \mathbf{P}_4 &= \boldsymbol{\varphi}_4^\top \mathbf{S}_4, \quad \mathbf{P}_{0,4} = \boldsymbol{\varphi}_4^\top \mathbf{S}_{0,4}, \quad \mathbf{Q}_4 = (\nabla \boldsymbol{\varphi}_4)^\top \mathbf{S}_4, \quad \mathbf{Q}_{0,4} = (\nabla \boldsymbol{\varphi}_4)^\top \mathbf{S}_{0,4}. \end{aligned} \quad (5.12)$$

⁴It is also viable to decouple the acoustic equations into a single second-order equation containing only \mathbf{u} as unknown. We choose to not do so because it would result in a damping matrix not diagonalizable by the mass or stiffness matrices. To fully decouple the system ODEs would then require doubling the DOFs (equivalent to 6 variables) to transform into a first-order system. This appears suboptimal to us as the original first-order system of acoustic equations has only 4 variables.

Then similar to (2.18), we find

$$\begin{aligned}
\sum_{j=1}^3 \mathbf{A}_{ij} \nabla u_j &= \mathbf{A}_i \mathbf{Q} \boldsymbol{\xi} + \mathbf{A}_i \mathbf{Q}_0 \boldsymbol{\xi}_0, \\
\sum_{j=1}^3 \mathbf{B}_{ij} \nabla u_j &= \mathbf{B}_i \mathbf{Q} \boldsymbol{\xi} + \mathbf{B}_i \mathbf{Q}_0 \boldsymbol{\xi}_0, \\
\partial_{x_i} p &= \partial_{x_i} \boldsymbol{\varphi}_4 \cdot \mathbf{S}_4 \boldsymbol{\xi} + \partial_{x_i} \boldsymbol{\varphi}_4 \cdot \mathbf{S}_{0,4} \boldsymbol{\xi}_0,
\end{aligned} \tag{5.13}$$

so that space partial derivatives can be expressed as linear transformations of the DOF vector $\boldsymbol{\xi}(t)$ or its time derivatives. It now suffices to derive the system of second-order ODEs similar to (2.19)–(2.20). We use \mathbf{P}_i^\top as a vector of test functions for the i th weak form equation in (5.8) and use \mathbf{P}_4^\top to test the weak form (5.10), which would yield 4 groups of equations, each group having N equations. Summing the 4 groups into 1 group, we derive a system of N coupled first-order ODEs as

$$\mathbf{M} \dot{\boldsymbol{\xi}}(t) + \mathbf{K} \boldsymbol{\xi}(t) = \mathbf{f}(t), \tag{5.14}$$

where

$$\begin{aligned}
\mathbf{M} &= \int_{\Omega} (\rho \mathbf{P}^\top \mathbf{P} + \mathbf{P}_4^\top \mathbf{P}_4) \, dV, \\
\mathbf{M}_0 &= \int_{\Omega} (\rho \mathbf{P}^\top \mathbf{P}_0 + \mathbf{P}_4^\top \mathbf{P}_{0,4}) \, dV, \\
\mathbf{K} &= \int_{\Omega} [\mathbf{Q}^\top (\mu_1 \mathbf{A} + \mu_2 \mathbf{B}) \mathbf{Q} + \rho c^2 \mathbf{P}_4^\top \mathbf{H} \mathbf{Q} + \mathbf{P}^\top \mathbf{Q}_4] \, dV, \\
\mathbf{K}_0 &= \int_{\Omega} [\mathbf{Q}^\top (\mu_1 \mathbf{A} + \mu_2 \mathbf{B}) \mathbf{Q}_0 + \rho c^2 \mathbf{P}_4^\top \mathbf{H} \mathbf{Q}_0 + \mathbf{P}^\top \mathbf{Q}_{0,4}] \, dV, \\
\mathbf{f}(t) &= \int_{\Omega} \mathbf{P}^\top \mathbf{F} \, dV - \mathbf{M}_0 \dot{\boldsymbol{\xi}}_0(t) - \mathbf{K}_0 \boldsymbol{\xi}_0(t).
\end{aligned} \tag{5.15}$$

Here \mathbf{M} and \mathbf{K} may not be as meaningful as the mass and stiffness matrices in the second-order ODEs case. The initial conditions are

$$\mathbf{u}|_{t=0} = \mathbf{0}, \quad p|_{t=0} = 0. \tag{5.16}$$

The acoustic space is often finite, which means boundary conditions are essential to shape the solutions of acoustic equations. Let $\Gamma^{(c)} \in \mathbb{R}^3$ be the acoustic space's whole solid boundary, of which $\Gamma_1^{(c)}, \Gamma_2^{(c)} \in \Gamma^{(c)}$ are the room boundary (grounds, walls, ceilings) and piano soundboard parts respectively, as shown in figure 4. In [11], the walls were assumed rigid, which can produce sound reflection effects but may miss sound absorption effects. This motivates our introduction of vibratory acoustic boundaries to account for various phenomena like reflection, scattering, absorption, diffusion, resonance etc.

5.2 Model for the room

In this section, we delve into the specification of room boundary models, which serve as the cornerstone for the subsequent analysis of solid-air coupling dynamics. For the sake of conciseness, we adopt a simplified representation of the room environment as a shoebox-shaped 3D space accommodating a piano. It is worth noting, however, that this room model remains versatile and can be readily adapted to accommodate irregular room geometries. The room's boundaries—encompassing floors, walls, and ceilings—play pivotal roles in shaping the acoustic behavior within, acting as both reflectors and absorbers of sound waves. In the context of physical modeling, these boundaries are treated as 3D elastic materials, akin to the piano's soundboard model. This methodological alignment facilitates the straight application of the general 3D elasticity model and the soundboard model to the room, obviating the need for reformulations of the governing equations and weak forms.

The primary specialization within this framework lies in the stipulation of boundary conditions of room barriers. As highlighted red in figure 4, the inner side of ground, wall and ceiling (blue color), defined as $\Gamma_1^{(f)}$, is the room material's interface with the air; the underside of ground

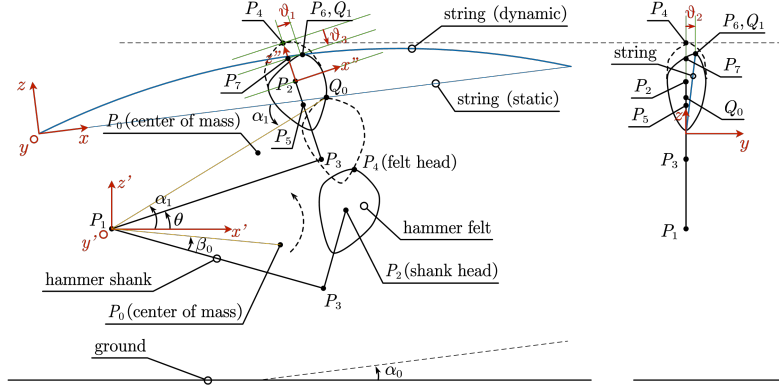


Figure 5: The piano hammer view from y (left) and x (right) direction

material (red color), defined as $\Gamma_2^{(f)}$, is where the Dirichlet boundary condition applies. Firmly rooted in the earth, the ground material should experience zero displacement along $\Gamma_2^{(f)}$. This condition is written as

$$\mathbf{u}^{(f)}|_{\mathbf{x} \in \Gamma_2^{(f)}} = \mathbf{0}. \quad (5.17)$$

In case the inner concrete layers of walls and ceilings are considered rigid, displacements on the surfaces of them should be zero too. Another specialization is that prestress need not be considered for room barriers. Even if it exists, the dynamic deformation may not be large enough to induce significant effect of prestress on vibration.

6 Model for coupling between different parts of the piano

6.1 Model for hammer-string coupling

The piano hammer positioned below the string functions the excitation of string vibration, which is known to be a highly nonlinear process [17]. We consider two main parts of the hammer relevant to this excitation process: the wooden hammer shank that can be approximated as non-deformable; the hammer felt that is deformable, impacting and exerting force on the string. Normally, the hammer moves in a circle when triggered by piano player's key action, striking the string at certain point in during a very short period of time, and is also pushed back by the vibrating string.

6.1.1 One hammer striking one string

For the case of one hammer striking one string, the study follows the 0D nonlinear hammer-string interaction model in [11], with some refinements: for the case of one hammer striking one string, the rotational movement of hammer [12] and the horizontal interaction force are taken into account.

As shown in figure 5, xyz is the coordinate system of piano string, where the x axis of the string system has an angle α_0 to the ground. To better describe the hammer shank motion which is rotation around point P_1 , we will not often the use the xyz system. Instead, we define a static coordinate system $x'y'z'$ with origin P_1 , y' axis the same as y axis, z' axis with negative direction the same as gravity, and x' axis perpendicular to the $y'O'z'$ plane. The motion of hammer shank as a rigid body can then be described as rotating around the y' axis and not moving in the y' direction. We can thus use a single variable $\theta(t)$, the angle of $\overrightarrow{P_1P_3}$ to the x' axis, to fully describe the hammer shank motion. The hammer shank drives the overall motion of the shank head P_2 and felt head P_4 . Nevertheless, when the felt head is in contact with the string's Q_0 point, it undergoes a compression $\boldsymbol{\vartheta} = [\vartheta_1, \vartheta_2, \vartheta_3]^T$ from P_4 to P_6 , which also overlaps with the dynamic string point Q_1 , which also contributes to its motion. To perform a reasonable orthogonal decomposition of this compression, we define a dynamic coordinate system $x''y''z''$ with origin P_3 , x'' axis with positive direction $\overrightarrow{P_5Q_0}$, y'' axis with positive direction the

same as y axis, and z'' axis with positive direction $\overrightarrow{P_5P_2}$. The hammer compression can then be decomposed onto the x'', y'', z'' axes as marked as $\vartheta_1, \vartheta_2, \vartheta_3$ respectively in figure 5.

Denote the displacement of string point Q_0 with coordinate $\mathbf{x}_0^{(a)}$ in the xyz system as $\mathbf{u}_0^{(a)} = \mathbf{u}^{(a)}(\mathbf{x}_0^{(a)}, t)$. Denote the lengths of $Q_0P_1, P_0P_1, P_1P_3, P_2P_3, P_1P_2, P_2P_4$ as $L, L_0, L_1, L_2, L_3, L_4$ respectively, and the angle of $\overrightarrow{P_1Q_0}$ to the x' axis as α_1 . Our geometric analysis finds the coordinates of Q_1 (equivalent to P_6 in case of compression) in the $x'y'z'$ system and $x''y''z''$ system, denoted $\mathbf{x}_1^{(a')}$ and $\mathbf{x}_1^{(a'')}$, are

$$\begin{aligned} \mathbf{x}_1^{(a')} &= \mathbf{r}_0 + \mathbf{R}_0 \mathbf{u}_0^{(a)}, \quad \mathbf{x}_1^{(a'')} = \mathbf{r} + \mathbf{R}(\theta) \mathbf{x}_1^{(a')}, \\ \mathbf{r}_0 &= \begin{bmatrix} L \cos \alpha_1 \\ 0 \\ L \sin \alpha_1 \end{bmatrix}, \quad \mathbf{R}_0 = \begin{bmatrix} \cos \alpha_0 & 0 & -\sin \alpha_0 \\ 0 & 1 & 0 \\ \sin \alpha_0 & 0 & \cos \alpha_0 \end{bmatrix}, \\ \mathbf{r} &= \begin{bmatrix} -L_1 \\ 0 \\ -L_2 \end{bmatrix}, \quad \mathbf{R}(\theta) = \begin{bmatrix} \cos \theta & 0 & \sin \theta \\ 0 & 1 & 0 \\ -\sin \theta & 0 & \cos \theta \end{bmatrix}. \end{aligned} \quad (6.1)$$

And converting $\mathbf{x}_1^{(a'')}$ to $\mathbf{x}_1^{(a')}$ results in

$$\begin{aligned} \mathbf{x}_1^{(a')} &= \mathbf{s}(\theta) + \mathbf{S}(\theta) \mathbf{x}_1^{(a'')}, \\ \mathbf{s}(\theta) &= \begin{bmatrix} L_1 \cos \theta - L_2 \sin \theta \\ 0 \\ L_1 \sin \theta + L_2 \cos \theta \end{bmatrix}, \quad \mathbf{S}(\theta) = \begin{bmatrix} \cos \theta & 0 & -\sin \theta \\ 0 & 1 & 0 \\ \sin \theta & 0 & \cos \theta \end{bmatrix}. \end{aligned} \quad (6.2)$$

As previously discussed, we assume Q_0 and P_2 is non-deformable whereas P_4 is deformable. This means when the hammer is in contact with string, P_4 moves to P_6 ; when contact is absent, the position of P_4 is determined by the shank but not the string. The condition to satisfy that the hammer is in contact with string should be $z_1^{(a'')} \leq L_4$, viz. the z'' direction distance between string point and shank head is less than the static thickness of hammer felt. The hammer felt compression is then

$$\vartheta(\theta) = \begin{cases} \mathbf{x}_1^{(a'')} - \mathbf{L}_4, & z_1^{(a'')} \leq L_4 \\ \mathbf{0}, & z_0^{(a'')} > L_4 \end{cases} \quad (6.3)$$

where $\mathbf{L}_4 = [0, 0, L_4]^\top$; negative value of ϑ_i means the hammer felt is compressed towards the negative direction of x''_i axis, and vice versa. Due to compression, the hammer felt exerts an interaction force $\mathbf{F}^{(a'')}(\theta) = [F_1^{(a'')}, F_2^{(a'')}, F_3^{(a'')}]^\top$ (in $x''y''z''$ system) on the string. Reciprocally, the hammer felt suffers $-\mathbf{F}^{(a'')}$ from the string according to Newton's third law⁵. Based on [11], the hammer-string interaction force in the x''_i axis is modeled as a nonlinear function of compression as

$$F_i^{(a'')} = -\text{sgn}(\vartheta_i) [k_i |\vartheta_i|^{p_i} + r_i k_i \partial_t (|\vartheta_i|^{p_i})], \quad i = 1, 2, 3, \quad (6.4)$$

where k_i is the stiffness of hammer felt; p_i is a positive exponent accounting for nonlinearity; r_i is the relaxation coefficient accounting for the hammer's hysteretic and dissipative behaviour; function $\text{sgn}(\cdot)$ returns the sign of a real number. Converting the interaction force to $x'y'z'$ and $x''y''z''$ coordinates yields $\mathbf{F}^{(a')} = \mathbf{S}(\theta) \mathbf{F}^{(a'')}$ and $\mathbf{F}^{(a)} = \mathbf{R}_0^\top \mathbf{F}^{(a')}$.

To couple the hammer force with string motion, we need equations in the $x'y'z'$ system governing the motion of hammer shank, a rigid body. Denote the coordinates of shank mass centre P_0 , shank rotation centre P_1 , shank head P_2 in the $x'y'z'$ system as $\mathbf{x}_0^{(d')}, \mathbf{x}_1^{(d')}, \mathbf{x}_2^{(d')}$ respectively. It can be found that $\mathbf{x}_0^{(d')} = [L_0 \cos(\beta_0 + \theta), 0, L_0 \sin(\beta_0 + \theta)]^\top$ and $\mathbf{x}_2^{(d')} = \mathbf{s}(\theta)$, where β_0 is the angle of $\overrightarrow{P_1P_0}$ to the $\overrightarrow{P_1P_3}$. Define the total mass and homogenous line density of the hammer shank as m, ρ . It can be found that $m = \rho(L_1 + L_2)$, and the axis-free position of

⁵Note that we ignore here the string's normal and tangent stress and prestress on the interaction surface exerting on the hammer felt (as well as the relevant strain on the string side), which should already be zero per the Neumann boundary condition specified in (2.14) if DOFs are given to string displacements on this surface. Even if they should not be zero, it is relatively acceptable to ignore them as they are probably less contributive than the hammer's compression force. Treating them as non-zero would require imposing Dirichlet boundary conditions on some relevant DOFs of the string's side, which is a computational challenge.

center of mass P_0 projected on P_1P_3 and P_2P_3 are $(\frac{1}{2}L_1^2 + L_1L_2)/(L_1 + L_2)$ and $\frac{1}{2}L_2^2/(L_1 + L_2)$ respectively. It is obvious that the shank as a rigid body suffers these forces: string reaction force $\mathbf{F}^{(d'')} = -\mathbf{F}^{(a'')}$ at P_2 ; a rotation constraint force at P_1 , which has zero torque with respect to the y' axis; gravity $[0, 0, -mg]^\top$ at P_0 , where g is the scalar gravitational acceleration. It follows that the total torque with respect to the y' axis is $mgL_0 \cos(\beta_0 + \theta) + \mathbf{l} \cdot \mathbf{F}^{(d'')}(\theta)$ (only 1 dimension of torque is needed here), where $\mathbf{l} = [L_2, 0, -L_1]^\top$; the moment of inertia with respect to the y'' axis, denoted I , is

$$I = \int_0^{L_1} \rho l^2 dl + \int_0^{L_2} \rho (l^2 + L_1^2) dl = \rho \left(\frac{1}{3}L_1^3 + \frac{1}{3}L_2^3 + L_1^2L_2 \right) \quad (6.5)$$

which does not depend on θ . Applying Newton's second law for rotation, the differential equation of hammer shank motion is

$$I\ddot{\theta} = -\mu\dot{\theta} + mgL_0 \cos(\beta_0 + \theta) + \mathbf{l} \cdot \mathbf{F}^{(d'')}(\theta), \quad (6.6)$$

where $-\mu\dot{\theta}$ is the simplified damping force. Here $t = 0$ is the moment when the felt head first contacts the string and compression is still zero, and initial angle and angular velocity at this time should be known.

From the aforementioned deductions, we can abstract the hammer-string interaction force $\mathbf{F}^{(e)}$ as a nonlinear operator $\mathcal{F}(\mathbf{u}_0^{(a)}, \theta) : (\mathbb{R}^3, \mathbb{R}) \rightarrow \mathbb{R}^3$. This force should be added to the rhs of (2.11) as a non-conservative force. Then, (2.11) and (6.6) forms 2 sets of coupled equations for 2 sets of variables $(\mathbf{u}^{(a)}, \theta)$, which provides a foundation for obtaining a solution theoretically. Due to the highly nonlinear nature of hammer-string coupling, particularly in that Taylor series approximation may not work well for potentially non-smooth functions in (6.4), it would be inappropriate to use the common perturbation method. In section 7.2 we shall introduce an explicit time discretization method to efficiently solve the hammer-string coupling.

6.1.2 One hammer striking two or three strings

The case of one hammer striking multiple, say three strings can simply be treated it as if three independent felt heads were striking their corresponding strings. Three independent interaction forces $\mathbf{F}_{i=1,2,3}^{(e')}$ are computed from three independent compressions. The string force exerted on the shank is the sum $\mathbf{F}^{(d')} = -\sum_{i=1}^3 \mathbf{F}_i^{(e')}$, assuming the 3 compression forces apply to the same point of shank head. However, this approach may lose the dynamic interaction between different striking points of the hammer felt.

A 3D hammer model may be more accurate in capturing the interplay of different hammer striking points and the different positions of compression forces. The hammer felt is now modeled as a 3D elastic material with space discretization. Two kinds of spacial boundaries consist in the hammer felt: one contains the felt's 3 potential contact points with the 3 strings, represented as $P_{4,i}$ with coordinates $\mathbf{x}_{4,i=1,2,3}^{(e'')}$; another is the contact surface $\Gamma_1^{(e'')} \in \mathbb{R}^2$ with the hammer shank. The hammer shank is considered as a rigid 3D object, which means no inner space discretization is needed for it. Above all, one needs to pay attention to the choice of coordinate system for the 3D geometry of felt. A recommended choice here is the dynamic $x''y''z''$ system, which eliminates the felt's rigid body movement component and is thus suitable for FEM computation. Also, displacement fields $\mathbf{u}^{(e'')}(x^{(e'')}, t)$ for hammer felt and $\mathbf{u}^{(d'')}(x^{(d'')}, t)$ for hammer shank need to be defined.

For more realistic modeling that the contact is dynamically distributed over a region rather than occurring at only some dimensionless points, readers can refer to appendix C which describes an iterative algorithm for contact problems directly integrated into FEM, supporting time-varying contact boundary and boundary coupling. Another more analytical (but also seems more simplified) approach for contact problems was introduced in [35], where additional dynamic variables including pressure, density, stiffness and damping of the contact surface along with their governing equations are formulated.

Derivation of the felt compression dynamics is now based on the 3D elastic material model and soundboard model previously introduced, without the need for modeling prestress. We first consider the boundary conditions needed for the felt model. Denote the coordinate of $Q_{1,i}$ in the $x''y''z''$ system as $\mathbf{x}_{1,i}^{(a'')}$, which can be computed similar to (6.1). To represent hammer felt

compression, Dirichlet boundary condition should be imposed on these 3 contact points as

$$\mathbf{u}^{(e'')}(\mathbf{x}_{4,i}^{(e'')}, t) = \begin{cases} \mathbf{x}_{1,i}^{(a'')} - \mathbf{x}_{4,i}^{(e'')}, & z_{1,i}^{(a'')} \leq L_4 \\ \mathbf{0}, & z_{1,i}^{(a'')} > L_4 \end{cases}, \quad (6.7)$$

where $z_{1,i}^{(a'')} \leq L_4$ means contact is present and otherwise not. This determined displacement would occur on the rhs of system ODEs like (2.19) as a source term. It is assumed without contact, not only $P_{4,i}$ but also the entire felt will not experience deformation; with contact, the position of $P_{4,i}$, i.e. $P_{6,i}$, is the same as $Q_{1,i}$, triggering motion and compression of the hammer felt. However, this assumption is a simplification that when the hammer felt leaves the string, its compression immediately recovers, and may result in a problem that Neumann boundary condition is not satisfied at $P_{4,i}$ when there is no contact. For a more accurate treatment of the contact boundary problem, readers can go to appendix C. There we describe an elastic-rigid 3D contact algorithm able to account for the time-varying contact surface and the time-varying switch between Dirichlet and Neumann boundary conditions, but with increased algorithmic complexity and numeric convergence uncertainty. As for another boundary $\Gamma_1^{(e'')}$ which interfaces the shank, Dirichlet boundary condition should be imposed on as

$$\mathbf{u}^{(e'')}(\mathbf{x}^{(e'')}, t) = \mathbf{0}, \quad \mathbf{x}^{(e'')} \in \Gamma_1^{(e'')}, \quad (6.8)$$

because the rigid shank should have no deformation.

We then consider the dynamics of string and shank impacted by the felt. At the contact point with string, the felt's nonzero surface forces $\mathbf{G}^{(e'')}(\mathbf{x}_{4,i}^{(e'')}, t)$ should be transmitted to the string as

$$\mathbf{F}_i^{(a)} = - \begin{bmatrix} 0 & Z_{12} & Z_{13} \\ Z_{12} & Z_{22} & Z_{23} \\ Z_{13} & Z_{23} & Z_{33} \end{bmatrix} \begin{bmatrix} 1 \\ 1 \\ 1 \end{bmatrix}, \\ \{Z_{ij}\} = \mathbf{R}_0^\top \mathbf{R}(\theta)^\top \mathbf{G}^{(e'')}(\mathbf{x}_{4,i}^{(e'')}, t) \mathbf{R}(\theta) \mathbf{R}_0, \quad (6.9)$$

where Z_{11} is not transmitted considering that the hammer felt seems to have no direct contact with the string's surface whose normal is in the x axis (longitudinal direction). As for the felt's surface force exerting on the shank along the boundary $\Gamma_1^{(e'')} = \Gamma_1^{(d'')}$, previous practice of directly transmitting the felt-string interaction force to the shank is not applicable here due to the 3D nature of felt and shank. For a point $\mathbf{x}^{(e'')} = \mathbf{x}^{(d'')}$ in $\Gamma_1^{(e'')}$, with $\mathbf{n}^{(e'')}(\mathbf{x}^{(e'')})$ as the outward normal of its tangent plane, the felt would exert a surface force

$$\mathbf{F}^{(d'')}(\mathbf{x}^{(d'')}, t) = -\mathbf{G}^{(e'')}(\mathbf{x}^{(e'')}, t) \mathbf{n}^{(e'')}(\mathbf{x}^{(e'')}) \quad (6.10)$$

on the shank. Then the total contribution of felt force to the torque of shank with respect to the y'' axis is

$$\begin{aligned} T_1(\theta) &= \int_{\Gamma_1^{(d')}} \left(\mathbf{E}_0 \mathbf{F}^{(d')}(\mathbf{x}^{(d')}, t) \cdot \mathbf{x}^{(d')} \right) dV \\ &= \int_{\Gamma_1^{(d'')}} \left[\mathbf{E}_0 \mathbf{S}(\theta) \mathbf{F}^{(d'')}(\mathbf{x}^{(d'')}, t) \cdot \left(\mathbf{s}(\theta) + \mathbf{S}(\theta) \mathbf{x}^{(d'')} \right) \right] dV \\ &= \int_{\Gamma_1^{(d'')}} \left[\mathbf{F}^{(d'')}(\mathbf{x}^{(d'')}, t) \cdot \left(\mathbf{l} + \mathbf{E} \mathbf{x}^{(d'')} \right) \right] dV, \end{aligned} \quad (6.11)$$

where

$$\mathbf{l} = \begin{bmatrix} L_2 \\ 0 \\ -L_1 \end{bmatrix}, \quad \mathbf{E}_0 = \begin{bmatrix} 0 & 0 & -1 \\ 0 & 0 & 0 \\ 1 & 0 & 0 \end{bmatrix}, \quad \mathbf{E} = \begin{bmatrix} 0 & 0 & 1 \\ 0 & 0 & 0 \\ -1 & 0 & 0 \end{bmatrix} \quad (6.12)$$

are constant quantities. Note that the only dependence of T_1 on θ , though not explicitly written, consists in $\mathbf{F}^{(d'')}(\mathbf{x}^{(d'')}, t)$, tracing back to the conversion from xyz to $x''y''z''$ for string displacements. The total contribution of gravity to the torque of shank with respect to the y'' axis is

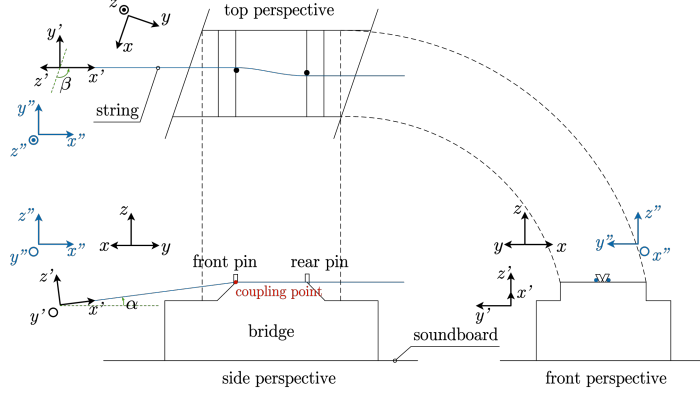


Figure 6: The piano bridge view from 3 directions

still $mgL_0 \cos(\beta_0 + \theta)$ if no relevant modifications are made when switching to the 3D hammer model. The moment of inertia with respect to the y'' axis, constant through time, is

$$I = \int_{\Omega^{(a')}} \rho (x^2 + z^2) dV, \quad (6.13)$$

where $\Omega^{(a')} \in \mathbb{R}^3$ is the shank's volume domain. Applying Newton's second law for rotation, the differential equation of hammer shank motion is

$$I\ddot{\theta} = -\mu\dot{\theta} + mgL_0 \cos(\beta_0 + \theta) + T_1(\theta). \quad (6.14)$$

Now the whole model of 3D hammer-string coupling has been established. The felt-string interaction force $\mathbf{F}_i^{(e)}$ in (6.9) is computed from the 3D hammer felt model with Dirichlet boundary conditions (6.7) (6.8), and added to the rhs of (2.11) as a non-conservative force. Then, (2.11) and (6.14) forms 2 sets of coupled equations for 2 sets of variables $(\mathbf{u}^{(a)}, \theta)$, which provides a foundation for obtaining a solution theoretically. Despite the linearity of 3D elasticity model, the felt's force on the string is still nonlinear because of the interaction judging condition.

6.2 Model for string-soundboard coupling

Piano strings are coupled to the soundboard's bridge part, which terminates and transmits string vibration to the soundboard. Figure 6 visualizes this coupling at the bridge from 3 perspectives, where xyz and $x'y'z'$ are the coordinate systems for soundboard and string respectively. Converting a vector (not a point) \mathbf{v} in the xyz system into \mathbf{v}' in the $x'y'z'$ system, according to the angles α and β marked in figure 6, yields $\mathbf{v}' = \mathbf{R}\mathbf{v}$ where $\mathbf{R} = \mathbf{R}_1\mathbf{R}_2$ and

$$\mathbf{R}_1 = \begin{bmatrix} \cos \alpha & 0 & \sin \alpha \\ 0 & 1 & 0 \\ -\sin \alpha & 0 & \cos \alpha \end{bmatrix}, \quad \mathbf{R}_2 = \begin{bmatrix} \cos \beta & \sin \beta & 0 \\ -\sin \beta & \cos \beta & 0 \\ 0 & 0 & 1 \end{bmatrix} \quad (6.15)$$

are the rotation matrices. The orthogonal property of rotation matrix yields $\mathbf{v} = \mathbf{R}^\top \mathbf{v}'$.

We conjecture from observations that the string-soundboard coupling is achieved via several mechanisms. The first mechanism is "bridge hump coupling", as illustrated in the side perspective of figure 6. The middle part of bridge is constructed a bit higher than the agraffe, the starting point of the speaking string. As a result, the string experiences some upward pressure from the bridge and the bridge experiences some downward pressure from the string, both statically and dynamically. The second mechanism is "bridge pin horizontal coupling", as illustrated in the top perspective of figure 6. Two bridge pins for one string are drilled into the bridge at positions that would bend the string a bit horizontally, bringing mutual horizontal tension between the string and bridge, and restricting the string's horizontal movement. Made of hard metal like steel, brass or even titanium, the bridge pins can be treated as rigid bodies with zero strain and stress. The third mechanism is "bridge pin vertical coupling", as illustrated in the front perspective of figure 6. The two bridge pins lean towards their respective string sides, blocking the string from

moving upwards beyond the pins. Also, the notches of bridge ensure that bridge hump coupling and bridge pin coupling occur at almost the same position, viz. the front bridge pin (the one closer to the agraffe).

On the string's side, the coupling point is defined as $\mathbf{x}_1^{(a)} = [L_1^{(a)}, 0, -r^{(a)}]^\top$, the lowest point of string at the front pin. While other relevant points for coupling may be $[L_1^{(a)}, -r^{(a)}, 0]^\top$, the closest point of string to the bridge pin, the string's displacements and surface forces at these points are identical, assuming $u^{(a)}$ does not vary with $y^{(a)}$ or $z^{(a)}$ at $x^{(a)} = L_1^{(a)}$ (no rotation) for simplicity⁶. The coordinate of this coupling point on the soundboard's side is denoted $\mathbf{x}_1^{(b)}$.

6.2.1 Static coupling

For coupling before motion is initiated, the string and soundboard should have non-zero prestress fields that attain static balance. It is sufficient to specify that the string prestress only acts perpendicular to its cross-sections and is constant through its speaking length. This means in the string's tension matrix $\mathbf{T}^{(a)}$, T_{11} is a constant and other entries are zero, immediately satisfying the static balance. For the soundboard, a full space dependent tension matrix $\mathbf{T}^{(b)}$ with 6 unique elements is necessary. The static balance condition can then be expressed as 3 partial differential equations

$$\nabla \cdot \mathbf{T}^{(b)} = \mathbf{0}, \quad (6.16)$$

which can be solved numerically by FEM using nodal surface forces as time-independent DOFs. Nonetheless, continuity between string and soundboard tension fields is required. To write the continuity equations, we define an intermediate coordinate system $x''y''z''$ resulting from rotating the $x'y'z'$ system by \mathbf{R}_1^\top or rotating the xyz system by \mathbf{R}_2 , as marked blue in figure 6. At the coupling point, the string's tension on surfaces with outward normals in the y'' and z'' axes exert on the bridge, whereas that in the x'' axis exerts on the farther hitch pins that seem to not connect the soundboard. This leads to one Dirichlet boundary condition for each string coupled to the soundboard as

$$\left(\mathbf{R}_2 \mathbf{T}^{(b)}(\mathbf{x}_1^{(b)}) \mathbf{R}_2^\top \right)_{[22,33,12,13,23]} = \left(\mathbf{R}_1^\top \mathbf{T}^{(a)}(\mathbf{x}_1^{(a)}) \mathbf{R}_1 \right)_{[22,33,12,13,23]}, \quad (6.17)$$

where subscript $_{[i_1, i_2, \dots]}$ means taking vector or matrix elements at indices i_1, i_2, \dots to form a vector. This condition can be deduced into 5 equations, leaving 1 DOF for the coupling point.

6.2.2 Dynamic coupling

For coupling in motion, the string transmits its surface forces (dynamic prestress, stress and damping force) to the soundboard. At coupling point, the string's total surface force, excluding the static prestress which is already accounted for on the soundboard's side, is $\mathbf{G}^{(a)}(\mathbf{x}_1, t)$. Similar to static coupling, only forces on surfaces with outward normals in the y'' and z'' axes are transmitted to the soundboard at the coupling point. This leads to

$$\mathbf{F}^{(b)}(\mathbf{x}^{(b)}, t) = \delta(\mathbf{x}^{(b)} - \mathbf{x}_1^{(b)}) \left(\mathbf{R}_2^\top \begin{bmatrix} 0 & Z_{12} & Z_{13} \\ Z_{12} & Z_{22} & Z_{23} \\ Z_{13} & Z_{23} & Z_{33} \end{bmatrix} \mathbf{R}_2 \right) \begin{bmatrix} 1 \\ 1 \\ 1 \end{bmatrix},$$

$$\{Z_{ij}\} = \mathbf{R}_1^\top \mathbf{G}^{(a)}(\mathbf{x}_1^{(a)}, t) \mathbf{R}_1, \quad (6.18)$$

where $\delta(\mathbf{x})$ is a 3D Dirac delta function indicating a point load. The above equations treats the string's surface force as a non-conservative force input to the soundboard system.

Another coupling condition arising from observation is that the string and soundboard should have the same y'' and z'' direction displacements⁷ at the coupling point, written as

$$\left(\mathbf{R}_1^\top \partial_t \mathbf{u}^{(a)}(\mathbf{x}_1^{(a)}, t) \right)_{[2,3]} = \left(\mathbf{R}_2 \partial_t \mathbf{u}^{(b)}(\mathbf{x}_1^{(b)}, t) \right)_{[2,3]}. \quad (6.19)$$

The reason for this is that the the aforementioned three coupling mechanisms constitute support for the string's surfaces with outward normals in the y'' and z'' axes at the coupling point. This

⁶This is also true for the string's central point $\mathbf{x}_1^{(a)} = [L_1^{(a)}, 0, 0]^\top$ previously defined.

⁷Here displacement continuity should be equivalent to velocity continuity, since both the string's and soundboard's displacements are based on a $[0, 0, 0]^\top$ point.

may not hold for the x'' axis, but if it is needed⁸, the subscript _[2,3] in above equations can be removed to impose a stronger displacement continuity condition. Anyway, restriction of the string's x'' axis (longitudinal) motion is always present at the farther hitch point which may not connect the soundboard, see (4.3). The same-displacement condition also provides a basis for establishing the string's displacement at the coupling point (Dirichlet boundary condition), so that the string's PDE (2.11) has an appropriate solution.

6.2.3 More discussions on coupling

String-soundboard coupling exhibits complex mechanisms that we find challenging to discover and describe. Some of these mechanisms that we observe but not covered in the aforementioned coupling model are discussed in this subsection. These discussions may not cover much details of computation due to their complexities.

Firstly, we only specified the coupling point at the bridge's front pin but ignored the rear pin. As coupling at the rear pin position potentially exists, the string in our model may need to be extended in length to cover the segment between the front pin position $\mathbf{x}_1 = [L_1^{(a)}, 0, -r^{(a)}]^\top$ and the rear pin position $\mathbf{x}_2 = [L_2^{(a)}, 0, -r^{(a)}]^\top$ (we call it "this segment" in this paragraph). At this segment, the horizontal bending of string may be accounted for in the prestress, but not necessarily represented in the geometrical volume for simplicity. In static state, the prestress field coupling should be computed for this segment paying attention that only at the two pin points are y'' axis surface forces coupled. In dynamic state, transmission of the string's surface forces should be computed for this segment, paying attention that only at the two pin points are y'' axis surface forces transmitted. A maybe more accurate computation of surface force transmission is, that at the two pins only when the string's y'' axis surface forces are towards the front or rear pins should they be transmitted, and that at between (excluding) the two pins only when the string's z'' axis surface forces are upwards should they be transmitted. This may lead to a highly nonlinear function akin to the case of hammer-string interaction (6.3), and may make imposing boundary conditions tougher due to the inequality rather than equality nature. For displacement coupling at this segment, at the two pins when the string's y'' direction displacements should not exceed the pins, whereas the z'' direction displacements are fully coupled to the pins; at between (excluding) the string's z'' direction displacements should not be under the soundboard plane, whereas the y'' direction displacements are unrestricted.

Secondly, we considered coupling as occurring at a point, but it may actually occur in a small contact surface (we call it "this surface" in this paragraph). In such a case, the Dirichlet boundary condition of prestress field coupling should be specified over this surface; the dynamic surface force transmission should be treated as surface load rather than point load; the Dirichlet boundary condition of displacement coupling should also be specified over this surface.

Thirdly, we still lack geometric details regarding the string's notable vertical and horizontal bending at the bridge. This bending changes the string's longitudinal direction, and thereby the 3 directions of vibration. Though string vibration should be terminated at the bridge pin, it seems only at the hitch pin that longitudinal vibration is fully restricted. Therefore, the string's segment from front bridge pin to hitch pin may require investigation, which may concern the duplex scale phenomena [25]. We can design a multi-segment geometric model for the string, each segment having differently rotated constitutive matrices. Also, the position-dependent static tension can be specified parallel to the central line of each string segment.

Finally, we ignored the soundboard's normal and tangent surface forces exerting on the string at coupling point. This is similar to the case of hammer-string coupling where the string's surface forces exerting on the hammer are ignored. This is mainly for practical considerations, as we would want to solve the soundboard's equations for only once. Since we did not impose Dirichlet boundary condition for the soundboard at each coupling point with the around 200 strings, Neumann boundary conditions apply here restricting the soundboard's conservative surface forces to be zero at coupling points. It may be acceptable given the intuitive feeling that "string \rightarrow soundboard" transmission should dominate "soundboard \rightarrow string" transmission. If the latter is essential, some DOFs may be need to be removed from the coupling point on the soundboard's

⁸Maybe in case of high enough viscosity or friction, the string can not slip more than the soundboard in the x'' direction. Restricting this movement may also make the solution of string's PDE more stable. This needs to be tested.

side, which is a challenge for imposing Dirichlet boundary condition reasonably for both the string and the soundboard.

6.3 Model for soundboard-air and room-air coupling

Modeling soundboard-air and room-air coupling is crucial for arriving at the final digital audio sound to the listeners. Generally in the context of solid-fluid coupling dynamics, the interaction surface should have continuous normal and tangential velocities, as well as continuous normal and tangential surface forces on both sides [19].

As per section 5, room-air coupling occurs on surface $\Gamma_1^{(f)}$ (room side) and $\Gamma_1^{(c)}$ (air side). Define coordinate transformation $\mathbf{x}^{(f)} = \mathbf{r}_1 + \mathbf{R}_1 \mathbf{x}^{(c)}$ from air coordinates to soundboard coordinates, where \mathbf{r}_1 and \mathbf{R}_1 are the shift vector and rotation matrix. We impose Dirichlet boundary condition of velocity continuity that

$$\mathbf{u}^{(c)}(\mathbf{x}^{(c)}, t) = \mathbf{R}_1^\top \dot{\mathbf{u}}^{(f)}(\mathbf{x}^{(f)}, t), \quad \mathbf{x}^{(c)} \in \Gamma_1^{(c)}, \quad \mathbf{x}^{(f)} = \mathbf{r}_1 + \mathbf{R}_1 \mathbf{x}^{(c)}. \quad (6.20)$$

We also specify the contribution of air surface force to the room equation's source term on the rhs of (2.11) as

$$\mathbf{F}_1^{(f)}(\mathbf{x}^{(f)}, t) = -\mathbf{G}^{(c)}(\mathbf{x}^{(c)}, t) \mathbf{n}^{(c)}(\mathbf{x}^{(c)}), \quad \mathbf{x}^{(f)} \in \Gamma_1^{(f)}, \quad \mathbf{x}^{(c)} = -\mathbf{R}_1^\top \mathbf{r}_1 + \mathbf{R}_1^\top \mathbf{x}^{(f)}, \quad (6.21)$$

where $\mathbf{n}^{(c)}(\mathbf{x}^{(c)})$ is the outward normal of the tangent plane of $\mathbf{x}^{(c)}$.

As per sections 3 and 5, soundboard-air coupling occurs on surface $\Gamma_2^{(b)}$ (soundboard side) and $\Gamma_2^{(c)}$ (air side). Define coordinate transformation $\mathbf{x}^{(b)} = \mathbf{r}_2 + \mathbf{R}_2 \mathbf{x}^{(c)}$ from air coordinates to soundboard coordinates, where \mathbf{r}_2 and \mathbf{R}_2 are the shift vector and rotation matrix. We impose Dirichlet boundary condition of velocity continuity that

$$\mathbf{u}^{(c)}(\mathbf{x}^{(c)}, t) = \mathbf{R}_2^\top \dot{\mathbf{u}}^{(b)}(\mathbf{x}^{(b)}, t), \quad \mathbf{x}^{(c)} \in \Gamma_2^{(c)}, \quad \mathbf{x}^{(b)} = \mathbf{r}_2 + \mathbf{R}_2 \mathbf{x}^{(c)}. \quad (6.22)$$

We also specify the contribution of air surface force to the soundboard equation's source term on the rhs of (2.11) as

$$\mathbf{F}_1^{(b)}(\mathbf{x}^{(b)}, t) = -\mathbf{G}^{(c)}(\mathbf{x}^{(c)}, t) \mathbf{n}^{(c)}(\mathbf{x}^{(c)}), \quad \mathbf{x}^{(b)} \in \Gamma_2^{(b)}, \quad \mathbf{x}^{(c)} = -\mathbf{R}_2^\top \mathbf{r}_2 + \mathbf{R}_2^\top \mathbf{x}^{(b)}, \quad (6.23)$$

where $\mathbf{n}^{(c)}(\mathbf{x}^{(c)})$ is the outward normal of the tangent plane of $\mathbf{x}^{(c)}$.

7 Numeric schemes

7.1 Modal superposition method for solving coupled ODEs

7.1.1 Modal transformation of second-order ODEs

For solving coupled second-order ODEs like (2.19), time discretization using finite-difference is a direct approach. However, given that damping matrix is diagonalizable by the mass and stiffness matrices, decoupling and dimension reduction of the system by means of modal superposition is preferred. To do so, we first define the following eigenvalue problem

$$\mathbf{K} \phi_i = \lambda_i \mathbf{M} \phi_i \iff \mathbf{M}^{-1} \mathbf{K} \phi_i = \lambda_i \phi_i \quad (i = 1, \dots, N), \quad (7.1)$$

and the eigen decomposition

$$\mathbf{K} = \mathbf{M} \Phi \Lambda \Phi^{-1} \iff \mathbf{M}^{-1} \mathbf{K} = \Phi \Lambda \Phi^{-1}, \quad (7.2)$$

where λ_i is a (maybe complex) eigenvalue, ϕ_i is a $N \times 1$ (maybe complex) eigenvector, $\Lambda = \text{diag}(\lambda_1, \dots, \lambda_N)$ is a diagonal matrix of eigenvalues, $\Phi = [\phi_1, \dots, \phi_N]$ is a $N \times N$ matrix of eigenvectors. Note that since both \mathbf{M} and \mathbf{K} are sparse matrices with large dimensions, it is preferable to solve the generalized eigenvalue problem on the left side of (7.1), avoiding explicit inversion of \mathbf{M} that would otherwise result in a large dense matrix. We can leverage existing softwares of sparse eigensolvers like Arpack and FEAST to solve the generalized eigenvalue problem. Nevertheless, for solving ODEs of the acoustic system with large DOFs, it may be

unwise to store all rows of eigenvectors at the same time which may otherwise lead to memory overload. A re-implementation of existing sparse eigensolver algorithms may be desired so as to store partial rows or columns of eigenvectors in a “rolling” way.

Since eigenvectors are linearly independent, that is to say Φ is invertible, we can write the solution in the form $\xi(t) = \Phi q(t)$ where $q(t)$ is an $N \times 1$ vector we call as modal DOFs. Note here $\xi(t)$ should be real (in the complex domain), but $q(t)$ may be complex because Φ^{-1} may be complex. Then (2.19) can be decoupled as

$$M\Phi\ddot{q}(t) + 2\mu K\Phi\dot{q}(t) + K\Phi q(t) = f(t) \quad (7.3a)$$

$$\Phi^H M\Phi\ddot{q}(t) + 2\mu\Phi^H K\Phi\dot{q}(t) + \Phi^H K\Phi q(t) = \Phi^H f(t) \quad (7.3b)$$

$$\bar{M}\ddot{q}(t) + 2\mu\bar{M}\Lambda\dot{q}(t) + \bar{M}\Lambda q(t) = \Phi^H f(t) \quad (7.3c)$$

$$\ddot{q}(t) + 2\mu\Lambda\dot{q}(t) + \Lambda q(t) = p(t) \quad (7.3d)$$

where

$$\bar{M} = \Phi^H M\Phi, \quad p(t) = \bar{M}^{-1}\Phi^H f(t); \quad (7.4)$$

are called the modal mass matrix and the modal force vector respectively. Through eigen decomposition, the N coupled ODEs have now been transformed into N uncoupled ODEs. Note that in case the damping matrix can not be diagonalized by the mass and stiffness matrices, we should rewrite the second-order ODEs as first-order ODEs with doubled number of DOFs, so that it can be decoupled as will be shown in section 7.1.2.

It is well-understood that the analytical solution of the i th uncoupled second-order ODE without the rhs nonhomogenous term is a sinusoidal signal with a single eigenfrequency positively correlated to the magnitude of i th eigenvalue. Assuming eigenvalues in Λ are ascendingly sorted by their real magnitudes, we can select only the lowest M eigenvalues and discard the rest, because most human ears are insensitive to eigenfrequencies above a certain threshold (often 10 kHz). This is also for practical considerations that the number of DOFs is often too large for numeric computation, making dimension reduction desirable. Consequently, we obtain a $M \times 1$ vector $q'(t)$ with only the first M entries of $q(t)$, and the $M + 1$ to N entries are all approximated as zeros and discarded. Substituting $q(t)$ by $q'(t)$ (more exactly, $q'(t)$ should be padded $N - M$ zeros at the end) in (7.3c), and omitting the last $N - M$ equations and unknowns, yields

$$S'\ddot{q}'(t) + 2\mu S'\Lambda'\dot{q}'(t) + S'\Lambda'q'(t) = \Phi'^T f(t) \quad (7.5a)$$

$$\ddot{q}'(t) + 2\mu\Lambda'\dot{q}'(t) + \Lambda'q'(t) = p'(t) \quad (7.5b)$$

where Λ' has dimension $M \times M$ containing the first M eigenvalues and Φ' has dimension $N \times M$ containing the first M eigenvectors. The large number of DOFs is now approximated as the linear combination of a smaller number of modal DOFs as $\xi(t) \approx \Phi'q'(t)$. The reduced modal mass and modal force are

$$\bar{M}' = \Phi'^H M\Phi', \quad p(t) = \bar{M}'^{-1}\Phi'^H f(t). \quad (7.6)$$

For around 2500 modes of the soundboard system as estimated in [10], the fully dense modal mass matrix (128 bit complex type) would require about 95 MB memory which is normally acceptable in both storage and computation aspects. But this dense matrix can be avoided if the mass and stiffness matrices are both symmetric because in this case the eigenvectors can be normalized so that the modal mass matrix equals to an identity matrix, making its inversion much easier. This benefit is achievable in our 3D elastic solid model because the constitutive matrix is symmetric even in the presence of prestress. A symmetric stiffness matrix often means that energy is conserved within the system if there is no other non-conservative forces like damping force.

Now we consider the analytical solution of the i th uncoupled nonhomogenous ODE

$$\ddot{q}(t) + 2\mu\lambda\dot{q}(t) + \lambda q(t) = p(t), \quad (7.7)$$

where the subscripts i and superscripts $'$ are dropped for convenience. Applying Laplace transform to this equation yields

$$\begin{aligned} s^2 Q(s) + 2\mu\lambda s Q(s) + \lambda Q(s) &= P(s) + Q_0(s), \\ s^2 G(s) + 2\mu\lambda s G(s) + \lambda G(s) - G_0(s) &= 1 \\ \ddot{q}(t) + 2\mu\lambda\dot{q}(t) + \lambda q(t) &= \delta(t) \end{aligned} \quad (7.8)$$

where s is a complex variable, $\delta(t)$ is the Dirac delta function; the initial parts of Laplace transforming derivatives are defined as

$$\begin{aligned} Q_0(s) &= sq(0) + \dot{q}(0) + 2\mu\lambda q(0) \\ G_0(s) &= sg(0) + \dot{g}(0) + 2\mu\lambda g(0); \end{aligned} \quad (7.9)$$

the well-known Green's function (frequency domain), the response to a unit impulse, is defined as

$$G(s) = \frac{Q(s) [1 + G_0(s)]}{P(s) + Q_0(s)} \Rightarrow Q(s) = \frac{G(s) [P(s) + Q_0(s)]}{1 + G_0(s)}. \quad (7.10)$$

To solve $g(t)$, we first specify that response should not exist during zero and negative time, viz. $g(t) = \dot{g}(t) = 0$ for $t \leq 0$; then notice when $t > 0$, (7.8) becomes homogenous with solution

$$g(t) = C_1 \exp(z_1 t) + C_2 \exp(z_2 t), \quad z_1, z_2 = -\mu\lambda \pm \sqrt{(\mu^2\lambda - 1)\lambda}.$$

To determine complex constants C_1, C_2 , we first notice that $g(t)$ should be continuous at $t = 0$ in the presence of second derivative in (7.8), thus

$$g(0^+) = g(0) \Rightarrow C_1 + C_2 = 0. \quad (7.11)$$

Then, integrating (7.8) over $(-\infty, +\infty)$ yields

$$\begin{aligned} \int_{-\infty}^{+\infty} [\ddot{g}(t) + 2\mu\lambda\dot{g}(t) + \lambda g(t)] dt &= \int_{-\infty}^{+\infty} \delta(t) dt \\ \Rightarrow \int_{0^-}^{0^+} \ddot{g}(t) dt &= \dot{g}(0^+) - \dot{g}(0^-) = \dot{g}(0^+) = 1 \\ \Rightarrow C_1 z_1 + C_2 z_2 &= 1, \end{aligned} \quad (7.12)$$

which is the so-called jump discontinuity condition for first derivative; the continuity condition for the zero-order has been applied again here. From (7.11) (7.12) the complex constants are found to be

$$C_1 = \frac{1}{z_1 - z_2}, \quad C_2 = \frac{1}{z_2 - z_1}. \quad (7.13)$$

Substituting $g(0) = 0$ and $\dot{g}(0) = 0$ into (7.9) yields $G_0(s) = 0$. Then from (7.10) we have

$$\begin{aligned} Q(s) &= P(s)G(s) + [\dot{q}(0) + 2\mu\lambda q(0)] G(s) + sq(0)G(s) \\ q(t) &= p(t) * g(t) + [\dot{q}(0) + 2\mu\lambda q(0)] g(t) + q(0)\dot{g}(t), \end{aligned} \quad (7.14)$$

where $*$ is the convolution operator over $[0, +\infty)$. For the general case of initial conditions $q(0) = \dot{q}(0) = 0$, the solution reduces to $q(t) = p(t) * g(t)$. It is now clear that the nonhomogenous ODEs can be solved by convolving the modal force $p(t)$ (source signal) with the Green's function $g(t)$ (response signal), which can be efficiently computed using fast Fourier transform (FFT) convolution in the frequency domain. However, the analytical solution may not be actually useful or efficient in the presence of coupling between systems and the explicit time discretization scheme introduced in section 7.2 will be an alternative. Nevertheless, it provides an understanding of the characteristics of vibration modes.

7.1.2 Modal transformation of first-order ODEs

Solving coupled first-order ODEs like (5.14) by means of modal superposition is similar to the second-order case, and we only discuss some particularities here. Firstly, the eigenvalue problem is defined in the same way for \bar{M} (now for first-order) and \bar{K} . The decoupled ODEs write

$$\bar{M}\dot{q}(t) + \bar{M}\Lambda q(t) = \Phi^H f(t) \quad (7.15a)$$

$$\dot{q}(t) + \Lambda q(t) = p(t) \quad (7.15b)$$

where

$$\bar{M} = \Phi^H M \Phi, \quad p(t) = \bar{M}^{-1} \Phi^H f(t) \quad (7.16)$$

are the modal mass and the modal force. Specific attention should be paid to the analytical solution of the i th uncoupled nonhomogenous ODE

$$\dot{q}(t) + \lambda q(t) = p(t). \quad (7.17)$$

Laplace transform yields

$$\begin{aligned} sQ(s) + \lambda Q(s) &= P(s) + q(0), \\ sG(s) + \lambda G(s) - g(0) &= 1 \\ \dot{g}(t) + \lambda g(t) &= \delta(t) \end{aligned} \quad (7.18)$$

where the Green's function is defined as

$$G(s) = \frac{Q(s)[1 + g(0)]}{P(s) + q(0)} \Rightarrow Q(s) = \frac{G(s)[P(s) + q(0)]}{1 + g(0)}. \quad (7.19)$$

Note that $g(t) = \dot{g}(t) = 0$ for $t \leq 0$ is still required, but continuity $g(0) = g(0^+)$ is unnecessary because the highest order of derivative in (7.18) is only one. Nevertheless, continuity of $\int g(t)dt$ at $t = 0$ can be easily satisfied because the primitive function can have an arbitrary constant added. Then integrating (7.18), we can find $g(0^+) = 1$ and the solution of Green's function

$$g(t) = -\frac{1}{\lambda} \exp(-\lambda t). \quad (7.20)$$

It follows that

$$\begin{aligned} Q(s) &= P(s)G(s) + q(0)G(s) \\ q(t) &= p(t) * g(t) + q(0)g(t), \end{aligned} \quad (7.21)$$

is the solution of the uncoupled nonhomogenous first-order ODE.

7.2 Explicit time discretization for coupling between systems

Having discussed the weak form ODEs for each subsystem of the physical piano, our question is then how a numerical treatment of coupling between system may be achieved that attains a sensible tradeoff between feasibility and accuracy. For most subsystems presented in the previous sections, there exists an external force term on the rhs of PDEs. This, along with the predetermined displacements on the boundary, form the main contributions to the rhs source term of system ODEs.

Nevertheless, to say ‘‘ODEs’’ here is actually indefensible, because in many coupling cases discussed before the rhs source term $\mathbf{f}(t)$ depends linearly or nonlinearly on the lhs unknown DOFs $\boldsymbol{\xi}(t)$ too. In such cases, eigen decomposition of ‘‘pseudo ODEs’’ can only obtain decoupled lhs operators on $\mathbf{q}(t)$ on the lhs, but rhs operators on $\mathbf{q}(t)$ often remain coupled, not only because of the nonlinearity of operators, but also because eigen decomposition applies to the local subsystem but not the global system where rhs sources come from. Hammer-string coupling is a typical example: the string displacement depends on the felt's force, the felt's force depends on its compression, but this compression depends on string displacement. Another example is in soundboard-string coupling, the soundboard displacement at the coupling point depends on the string's surface force, the string's surface force depends on its displacement, computing its displacement requires knowing the coupling point displacement (Dirichlet boundary), but this displacement depends on the soundboard displacement at the coupling point to satisfy the continuity condition.

An explanation for these seemingly odd relations is that a theoretically sound way would seem to do computations as if all subsystems were a single system, rather than to separate systems and reintroduce coupling between them. This means all DOFs are integrated into a single vector of DOFs, all mass (or stiffness) matrices are assembled into a bigger one, displacements at coupling positions are expressed by the same unique DOFs behind, in order for full coupling solutions. However, this is often unacceptable not only because of the high costs of storage and computation, but also because the inherent heterogeneities of different subsystems, particularly the nonlinearity of hammer felt compression, the first-order characteristic of acoustic system, the

different damping mechanisms, may actually not cohere well and may even be tough to control in a single system. Therefore, we shall still adopt the framework of separate systems with mutual coupling, and seek for numeric schemes capable of achieving a level of accuracy as close to full coupling schemes as possible.

The time domain scheme we shall introduce here is inspired by the idea of velocity Verlet algorithms, but customized for our case of modal-transformed first and second order ODEs, with second-order accuracy⁹. Despite being lower-order compared to the complex time schemes in [14, 8], our scheme may be more efficient particularly in eliminating the need to invert or solve big or dense matrices at each step, even when the mass matrix is non-diagonal. Due to the existence of coupling, the analytical solutions of first and second order ODEs discussed in section 7.1 may be not applicable here. Nevertheless, system decoupling and dimension reduction via modal decomposition will be shown useful in improving the efficiency of time-stepping algorithms.

7.2.1 Time stepping of second-order ODEs

In the previously derived second-order decoupled ODEs (7.3d), the rhs source term can be rewritten as

$$\ddot{\mathbf{q}}(t) + 2\mu\Lambda\dot{\mathbf{q}}(t) + \Lambda\mathbf{q}(t) = \mathbf{p}(t), \quad \mathbf{p}(t) = \mathbf{r}(t, \mathbf{q}(t), \dot{\mathbf{q}}(t)), \quad (7.22)$$

where \mathbf{r} incorporate all DOF-independent and DOF-dependent contributions to the source term; DOF-dependent contributions consist of two major sources: non-zero Dirichlet boundary conditions; non-conservative force (but excluding damping force already on the lhs).

To perform time discretization, we define the discrete time interval as $h = \Delta t$, which can be chosen as 1/44100 seconds for producing 44.1 kHz digital audio; define the n th discrete point in time as $t_n = nh$. The notion of discrete points in time form the basis of time stepping algorithms, where integrations are performed between time steps. An integral over a small interval $[x_0, x_0 + \Delta x]$ can be approximated as area of trapezium

$$\int_{x_0}^{x_0+h} f(x)dx \approx \frac{h}{2} [f(x_0) + f(x_0 + h)], \quad (7.23)$$

which can achieve a relatively high accuracy as per the mean value theorem for definite integrals, though $f(x_0 + h)$ may not be known beforehand in some contexts. If we seek for a first-order approximation of $f(x_0 + h)$, then

$$\int_{x_0}^{x_0+h} f(x)dx \approx hf(x_0) + \frac{h^2}{2}f'(x_0) \quad (7.24)$$

is a less accurate approximation. Utilizing these integration strategies, we integrate (7.22) over $[t_n, t_{n+1}]$ to get

$$\begin{aligned} \dot{\mathbf{q}}(t_{n+1}) - \dot{\mathbf{q}}(t_n) &= -2\mu\Lambda [\mathbf{q}(t_{n+1}) - \mathbf{q}(t_n)] - s\Lambda \int_{t_n}^{t_{n+1}} \mathbf{q}(t)dt + \int_{t_n}^{t_{n+1}} \mathbf{p}(t)dt \\ \dot{\mathbf{q}}(t_{n+1}) - \dot{\mathbf{q}}(t_n) &\approx -2\mu\Lambda [\mathbf{q}(t_{n+1}) - \mathbf{q}(t_n)] - \frac{h}{2}\Lambda [\mathbf{q}(t_n) + \mathbf{q}(t_{n+1})] + h\mathbf{p}(t_n) + \frac{h^2}{2}\dot{\mathbf{p}}(t_n). \end{aligned} \quad (7.25)$$

Also it is obvious that

$$\mathbf{q}(t_{n+1}) - \mathbf{q}(t_n) = \int_{t_n}^{t_{n+1}} \dot{\mathbf{q}}(t)dt \approx \frac{h}{2} [\dot{\mathbf{q}}(t_n) + \dot{\mathbf{q}}(t_{n+1})]. \quad (7.26)$$

The solution of (7.25) (7.26) is

$$\begin{aligned} \mathbf{q}(t_{n+1}) &= \mathbf{Z}_1^{-1} \left[\mathbf{Z}_0\mathbf{q}(t_n) + 2\dot{\mathbf{q}}(t_n) + h\mathbf{p}(t_n) + \frac{h^2}{2}\dot{\mathbf{p}}(t_n) \right], \\ \dot{\mathbf{q}}(t_{n+1}) &= \frac{2}{h}\mathbf{q}(t_{n+1}) - \frac{2}{h}\mathbf{q}(t_n) - \dot{\mathbf{q}}(t_n), \end{aligned} \quad (7.27)$$

⁹Alternatively, one may consider transforming time domain into frequency domain to explore coupling from the perspective of mobility [34].

where

$$\begin{aligned}\mathbf{Z}_0 &= \frac{2}{h}\mathbf{I} + \left(2\mu - \frac{h}{2}\right)\mathbf{\Lambda}, \\ \mathbf{Z}_1 &= \frac{2}{h}\mathbf{I} + \left(2\mu + \frac{h}{2}\right)\mathbf{\Lambda}.\end{aligned}\tag{7.28}$$

are diagonal matrices easy to invert. (7.27) reveal that $\mathbf{q}(t_{n+1})$, $\dot{\mathbf{q}}(t_{n+1})$ can be computed with second-order accuracy using $\mathbf{q}(t_n)$, $\dot{\mathbf{q}}(t_n)$, $\mathbf{p}(t_n)$, $\dot{\mathbf{p}}(t_n)$, but without using unknowns of the t_{n+1} step. This means our time discretization scheme is explicit. As for its energy property, readers can go to appendix D for a detailed deduction incorporating nonlinear strain energy. From the deduction there, our preliminary judgement is that this explicit scheme is energy stable at least for the kinetic energy, potential energy and damping, but uncertain for other non-conservative forces on the rhs. The most significant accuracy loss of this scheme seems to be the use of (7.24) rather than (7.23) in approximating the integral of $\mathbf{p}(t)$, which may also lead to energy unstability. We would expect the first-order approximation of $\mathbf{p}(t_{n+1})$ to be acceptable with small h . This actually implies that we rely on some historical (t_n) displacement and velocity values to predict the current (t_{n+1}) input sources, then the current input sources are updated by the computed current displacement and velocity values. This process can be repeated several times for one time step if higher accuracy and better energy stability is desired, able to use (7.23) rather than (7.24) in approximating the integral of $\mathbf{p}(t)$.

7.2.2 Time stepping of first-order ODEs

Recall the previously derived first-order decoupled ODEs (7.15b), the rhs source term can be rewritten as

$$\dot{\mathbf{q}}(t) + \mathbf{\Lambda}\mathbf{q}(t) = \mathbf{p}(t), \quad \mathbf{p}(t) = \mathbf{r}(t, \mathbf{q}(t)),\tag{7.29}$$

where \mathbf{r} incorporate all DOF-independent and DOF-dependent contributions to the source term; DOF-dependent contributions consist of two major sources: non-zero Dirichlet boundary conditions; non-conservative force (but excluding damping force already on the lhs). Integrating (7.29) over $[t_n, t_{n+1}]$, the approximate solution of $\mathbf{q}(t_{n+1})$ can be found as

$$\begin{aligned}\mathbf{q}(t_{n+1}) - \mathbf{q}(t_n) &= -\mathbf{\Lambda} \int_{t_n}^{t_{n+1}} \mathbf{q}(t)dt + \int_{t_n}^{t_{n+1}} \mathbf{p}(t)dt \\ \mathbf{q}(t_{n+1}) - \mathbf{q}(t_n) &\approx -\frac{h}{2}\mathbf{\Lambda} [\mathbf{q}(t_n) + \mathbf{q}(t_{n+1})] + h\mathbf{p}(t_n) + \frac{h^2}{2}\dot{\mathbf{p}}(t_n) \\ \mathbf{q}(t_{n+1}) &= \left(\mathbf{I} + \frac{h}{2}\mathbf{\Lambda}\right)^{-1} \left[\left(\mathbf{I} - \frac{h}{2}\mathbf{\Lambda}\right) \mathbf{q}(t_n) + h\mathbf{p}(t_n) + \frac{h^2}{2}\dot{\mathbf{p}}(t_n) \right].\end{aligned}\tag{7.30}$$

Therefore, $\mathbf{q}(t_{n+1})$ can be computed using $\mathbf{q}(t_n)$, $\mathbf{p}(t_n)$, $\dot{\mathbf{p}}(t_n)$, but without using unknowns of the t_{n+1} step.

7.2.3 Time stepping of hammer shank rotation ODE

The equation of hammer shank motion (6.14) can be written in a more abstract way as

$$I\ddot{\theta} = -\mu\dot{\theta} + T(\theta),\tag{7.31}$$

where $T(\theta)$ incorporate the contributions of gravity and felt force to the total torque of shank, dependent on the zero-order value of θ . Similar to second-order system ODEs, the time discretization of (7.31) is found to be

$$\begin{aligned}I \left[\dot{\theta}(t_{n+1}) - \dot{\theta}(t_n) \right] &= -\mu [\theta(t_{n+1}) - \theta(t_n)] + \int_{t_n}^{t_{n+1}} T(\theta)dt \\ I \left[\frac{2}{h}\theta(t_{n+1}) - \frac{2}{h}\theta(t_n) - 2\dot{\theta}(t_n) \right] &\approx -\mu [\theta(t_{n+1}) - \theta(t_n)] + hT(t_n) + \frac{h^2}{2}\dot{T}(t_n) \\ \theta(t_{n+1}) &= \left(\frac{2}{h}I + \mu\right)^{-1} \left[\left(\frac{2}{h}I + \mu\right) \theta(t_n) + 2\dot{\theta}(t_n) + hT(t_n) + \frac{h^2}{2}\dot{T}(t_n) \right],\end{aligned}\tag{7.32}$$

and

$$\dot{\theta}(t_{n+1}) = \frac{2}{h}\theta(t_{n+1}) - \frac{2}{h}\theta(t_n) - \dot{\theta}(t_n). \quad (7.33)$$

Therefore, $\theta(t_{n+1})$ and $\dot{\theta}(t_{n+1})$ can be computed using $\theta(t_n)$, $\dot{\theta}(t_n)$, $T(t_n)$, $\dot{T}(t_n)$, but without using unknowns of the t_{n+1} step.

7.3 Concatenating the whole model

With modal transformation and time discretization of the ODEs established, it now suffices to combine all parts of the piano model together. The whole computation process consists of two major separate parts: first do space discretization, then do time discretization. Rooted in the time-space separation idea of FEM, these two numeric works do not interfere so computation costs should be acceptable.

7.3.1 Space discretization

Derive ODEs for each subsystem.

$$\begin{aligned} M\ddot{\xi}(t) + C\dot{\xi}(t) + K\xi(t) &= \mathbf{f}(t), \text{ superscripts : } a, b, e, f \\ M\dot{\xi}(t) + K\xi(t) &= \mathbf{f}(t), \text{ superscripts : } c \\ \ddot{\theta} &= -\mu\dot{\theta} + T(\theta), \text{ superscripts : } d \end{aligned}$$

Solve generalized eigenvalue problems. Only find the lowest M eigenvalues and corresponding eigenvectors, and integrate them into Λ , Φ .

$$K\phi_i = \lambda_i M\phi_i, \quad i = 1, \dots, M, \text{ superscripts : } a, b, c, e, f$$

Compute modal force transformation matrix (dense). This is useful for transformation $\mathbf{p}(t) = S\mathbf{f}(t)$.

$$S = \left(\Phi^H M \Phi \right)^{-1} \Phi^H, \text{ superscripts : } a, b, c, e, f$$

7.3.2 Time discretization

Update schemes for modal DOFs Below lists the previously introduced time discretization schemes to be later referred to. For each time step n , schemes 1a/2a/3a are preferred over 1b/2b/3b whenever possible, because they utilize values of the rhs source term for next time step $n+1$.

- Update scheme 1a:

$$\mathbf{q}(t_{n+1}) = \left(\mathbf{I} + \frac{h}{2}\Lambda \right)^{-1} \left[\left(\mathbf{I} - \frac{h}{2}\Lambda \right) \mathbf{q}(t_n) + \frac{h}{2}\mathbf{p}(t_n) + \frac{h}{2}\mathbf{p}(t_{n+1}) \right]$$

- Update scheme 1b:

$$\mathbf{q}(t_{n+1}) = \left(\mathbf{I} + \frac{h}{2}\Lambda \right)^{-1} \left[\left(\mathbf{I} - \frac{h}{2}\Lambda \right) \mathbf{q}(t_n) + h\mathbf{p}(t_n) + \frac{h^2}{2}\dot{\mathbf{p}}(t_n) \right]$$

- Update scheme 2a:

$$\begin{aligned} \mathbf{q}(t_{n+1}) &= \mathbf{Z}_1^{-1} \left[\mathbf{Z}_0 \mathbf{q}(t_n) + 2\dot{\mathbf{q}}(t_n) + \frac{h}{2}\mathbf{p}(t_n) + \frac{h}{2}\mathbf{p}(t_{n+1}) \right] \\ \dot{\mathbf{q}}(t_{n+1}) &= \frac{2}{h}\mathbf{q}(t_{n+1}) - \frac{2}{h}\mathbf{q}(t_n) - \dot{\mathbf{q}}(t_n) \end{aligned}$$

- Update scheme 2b:

$$\mathbf{q}(t_{n+1}) = \mathbf{Z}_1^{-1} \left[\mathbf{Z}_0 \mathbf{q}(t_n) + 2\dot{\mathbf{q}}(t_n) + h\mathbf{p}(t_n) + \frac{h^2}{2}\dot{\mathbf{p}}(t_n) \right]$$

$$\dot{\mathbf{q}}(t_{n+1}) = \frac{2}{h}\mathbf{q}(t_{n+1}) - \frac{2}{h}\mathbf{q}(t_n) - \dot{\mathbf{q}}(t_n)$$

- Update scheme 3a:

$$\theta(t_{n+1}) = \left(\frac{2}{h}I + \mu \right)^{-1} \left[\left(\frac{2}{h}I + \mu \right) \theta(t_n) + 2\dot{\theta}(t_n) + \frac{h}{2}T(t_n) + \frac{h^2}{2}\dot{T}(t_n) \right]$$

$$\dot{\theta}(t_{n+1}) = \frac{2}{h}\theta(t_{n+1}) - \frac{2}{h}\theta(t_n) - \dot{\theta}(t_n)$$

- Update scheme 3b:

$$\theta(t_{n+1}) = \left(\frac{2}{h}I + \mu \right)^{-1} \left[\left(\frac{2}{h}I + \mu \right) \theta(t_n) + 2\dot{\theta}(t_n) + hT(t_n) + \frac{h^2}{2}\dot{T}(t_n) \right]$$

$$\dot{\theta}(t_{n+1}) = \frac{2}{h}\theta(t_{n+1}) - \frac{2}{h}\theta(t_n) - \dot{\theta}(t_n)$$

Initialization

1. Discrete time interval h , number of time steps n_1 .
2. Hammer shank: initial angle and angular velocity $\theta^{(d')}(t_0)$, $\dot{\theta}^{(d')}(t_0)$, from which the initial torque $T^{(d')}(t_0)$ and its derivative $\dot{T}^{(d')}(t_0)$ (gravity contribution only) can be computed.
3. Hammer felt & string & soundboard & air & room barriers: initial modal DOFs and modal forces

$$\mathbf{q}^{(*)}(t_0) = \dot{\mathbf{q}}^{(*)}(t_0) = \mathbf{p}^{(*)}(t_0) = \dot{\mathbf{p}}^{(*)}(t_0) = \mathbf{0}, \quad * = a, b, c, e'', f$$

At each time step $n = 0, 1, 2, \dots, n_1$

1. Compute the next rotation of hammer shank using scheme 3b:

$$\theta^{(d')}(t_n), \dot{\theta}^{(d')}(t_n), T^{(d')}(t_n), \dot{T}^{(d')}(t_n) \rightarrow \theta^{(d')}(t_{n+1}), \dot{\theta}^{(d')}(t_{n+1})$$

2. Compute the current modal forces of hammer felt (non-zero boundary condition) using (6.7):

$$\theta^{(d')}(t_n), \dot{\theta}^{(d')}(t_n), \mathbf{q}^{(a)}(t_n), \dot{\mathbf{q}}^{(a)}(t_n) \rightarrow \mathbf{p}^{(e'')}(t_n), \dot{\mathbf{p}}^{(e'')}(t_n)$$

Note: $\mathbf{p}^{(e'')}(t_n)$ relates to the displacement of felt at the contact points with string. The algorithm in appendix C may be more accurate for the hammer felt, but for simplicity we choose to not integrate it here.

3. Compute the next modal DOFs of hammer felt using scheme 2b:

$$\mathbf{q}^{(e'')}(t_n), \dot{\mathbf{q}}^{(e'')}(t_n), \mathbf{p}^{(e'')}(t_n), \dot{\mathbf{p}}^{(e'')}(t_n) \rightarrow \mathbf{q}^{(e'')}(t_{n+1}), \dot{\mathbf{q}}^{(e'')}(t_{n+1})$$

4. Compute the next torque of hammer shank using (6.14):

$$\theta^{(d')}(t_{n+1}), \dot{\theta}^{(d')}(t_{n+1}), \mathbf{q}^{(e'')}(t_{n+1}), \dot{\mathbf{q}}^{(e'')}(t_{n+1}) \rightarrow T^{(d')}(t_{n+1}), \dot{T}^{(d')}(t_{n+1})$$

5. Compute the next modal forces of string (non-conservative force) using (6.9):

$$\mathbf{q}^{(e'')}(t_{n+1}) \rightarrow \mathbf{p}_1^{(a)}(t_{n+1})$$

Note: $\mathbf{p}_1^{(a)}$ relates to hammer felt force, $\mathbf{p}_2^{(a)}$ relates to bridge point displacement.

6. Compute the next modal DOFs of string using scheme 2a for $\mathbf{p}_1^{(a)}$ and scheme 2b for $\mathbf{p}_2^{(a)}$:

$$\mathbf{q}^{(a)}(t_n), \dot{\mathbf{q}}^{(a)}(t_n), \mathbf{p}_1^{(a)}(t_n), \mathbf{p}_1^{(a)}(t_{n+1}), \mathbf{p}_2^{(a)}(t_n), \dot{\mathbf{p}}_2^{(a)}(t_n) \rightarrow \mathbf{q}^{(a)}(t_{n+1}), \dot{\mathbf{q}}^{(a)}(t_{n+1})$$

7. Compute the next modal forces of soundboard (non-conservative force) using (6.18):

$$\mathbf{q}^{(a)}(t_{n+1}) \rightarrow \mathbf{p}_1^{(b)}(t_{n+1})$$

Note: $\mathbf{p}_1^{(b)}$ relates to string force at the bridge, $\mathbf{p}_2^{(b)}$ relates to air pressure on the soundboard.

8. Compute the next modal DOFs of soundboard using scheme 2a for $\mathbf{p}_1^{(b)}$ and scheme 2b for $\mathbf{p}_2^{(b)}$:

$$\mathbf{q}^{(b)}(t_n), \dot{\mathbf{q}}^{(b)}(t_n), \mathbf{p}_1^{(b)}(t_n), \mathbf{p}_1^{(b)}(t_{n+1}), \mathbf{p}_2^{(b)}(t_n), \dot{\mathbf{p}}_2^{(b)}(t_n) \rightarrow \mathbf{q}^{(b)}(t_{n+1}), \dot{\mathbf{q}}^{(b)}(t_{n+1})$$

9. Compute the next modal forces of air (non-zero boundary condition) using (6.22):

$$\mathbf{q}^{(b)}(t_{n+1}) \rightarrow \mathbf{p}_1^{(c)}(t_{n+1})$$

Note: $\mathbf{p}_1^{(c)}$ relates to displacements at the interface with soundboard, $\mathbf{p}_2^{(c)}$ relates to displacements at interface with room barriers.

10. Compute the next modal DOFs of air using scheme 1a for $\mathbf{p}_1^{(c)}$ and scheme 1b for $\mathbf{p}_2^{(c)}$:

$$\mathbf{q}^{(c)}(t_n), \mathbf{p}_1^{(c)}(t_n), \mathbf{p}_1^{(c)}(t_{n+1}), \mathbf{p}_2^{(c)}(t_n), \dot{\mathbf{p}}_2^{(c)}(t_n) \rightarrow \mathbf{q}^{(c)}(t_{n+1})$$

11. Compute the next modal forces of soundboard (non-conservative force) using (6.23):

$$\mathbf{q}^{(c)}(t_{n+1}) \rightarrow \mathbf{p}_2^{(b)}(t_{n+1}), \dot{\mathbf{p}}_2^{(b)}(t_{n+1})$$

12. Compute the next modal forces of room barriers (non-conservative force) using (6.21):

$$\mathbf{q}^{(c)}(t_{n+1}) \rightarrow \mathbf{p}^{(f)}(t_{n+1})$$

Note: $\mathbf{p}^{(e'')}(t_n)$ relates to air pressure on the room barriers.

13. Compute the next modal DOFs of room barriers using scheme 2a:

$$\mathbf{q}^{(f)}(t_n), \dot{\mathbf{q}}^{(f)}(t_n), \mathbf{p}^{(f)}(t_n), \mathbf{p}^{(f)}(t_{n+1}) \rightarrow \mathbf{q}^{(f)}(t_{n+1}), \dot{\mathbf{q}}^{(f)}(t_{n+1})$$

14. Compute the next modal forces of air (non-zero boundary condition) using (6.20):

$$\mathbf{q}^{(f)}(t_{n+1}), \dot{\mathbf{q}}^{(f)}(t_{n+1}) \rightarrow \mathbf{p}_2^{(c)}(t_{n+1}), \dot{\mathbf{p}}_2^{(c)}(t_{n+1})$$

15. If higher accuracy and better energy stability is desired, repeat the above steps 1 to 14 several times. Note that different from the first iteration, the subsequent iterations always use schemes 1a, 2a, 3a and do not need to use schemes 1b, 2b, 3b. If no more repetition is needed, end the current time step and move on to the next time step.

Audio output Compute the acoustic pressure signals at certaining listening positions using the stored modal DOFs $\mathbf{q}^{(c)}(t_n)$ ($n = 0, \dots, n_1$) and modal superposition. These signals are the final output digital audio of piano simulation model.

8 Conclusion

This paper presented a detailed physical model for simulating acoustic piano sounds. For solid parts of the piano system, viz. strings, soundboard, room barriers, hammer felt, a 3D prestressed elasticity model is generally applied. For fluid parts of the piano system, viz. sound radiation in the air, conservation of mass and Navier-Stokes equation is applied. For coupling between different subsystems of the piano, mechanisms of surface force transmission and displacement/velocity continuity are considered. For numeric simulation, modal superposition and explicit time discretization schemes are utilized. Despite the complexity of this whole piano model, we have paid efforts to a straightforward presentation based more on system ODEs transformed from strong PDEs, as well as a time domain simulation scheme balancing efficiency and accuracy.

Below discusses the current study's limitations and our plans or recommendations for future research.

- Waiting for numeric simulation results. Due to the complication of our piano model, we choose to write down theoretic models first as a guiding framework. Our next step involves implementing the computation procedures using high-performance, expressive and well-structured programming languages like Rust, as well as performing result analysis using convenient and ecologically rich programming languages like Python. Facing some unknown uncertainties in practice, our model needs to be further tested and improved.
- In hammer felt-string coupling and string-soundboard coupling, the contact was treated as occurring at a point rather than an area. This simplification would probably lead to a loss in realism. The 3D contact framework described in appendix C may apply here, but algorithmic complexity and numeric stability needs to be better addressed.
- The string-soundboard coupling mechanism was assumed of fixation but not collision nature. A coupling model similar to the nonlinear hammer-string interaction may be more suitable, considering that a string seems to actually be supported between two distanced bridge pins. The 3D contact framework described in appendix C may apply here, but algorithmic complexity and numeric stability needs to be better addressed. It also remains to discover how the relative positions of the two pins affect the vibrations of the string and soundboard.
- Treatment of nonlinear coupling between the distinct subsystems of the piano in time discretization schemes remains challenging. As far as we understand, only nonlinear implicit schemes can achieve unconditional energy stability if the two coupling mechanisms we consider, namely the surface force transmission and the displacement/velocity continuity, exhibit nonlinearity. A viable tradeoff between accuracy and efficiency may be the explicit iteration approach we proposed, but we hope to see better alternatives.
- The damping in our model is relatively simplified, as only one or two viscosity coefficients are used. It may be beneficial to introduce additional unknowns like temperature and additional governing equations like thermal equations to reflect the damping phenomena more realistically.
- Some observed phenomena of acoustic pianos are still missing their representations in our model. For example, strings not struck by the hammer may also vibrate as long as the sustain pedal is pressed, which is often called sympathetic resonance. An explanation for this is that the struck string transmits its vibration to other strings through the variation of air pressure, which can actually lead to a string-air coupling model. Also, the transmission of piano player's key action into hammer shank movement requires further investigation.
- It remains to discover the relation between physical parameters of the piano model and the objective (waveforms, spectrums) and subjective (listener feel) aspects of the final output sound, so that these parameters can be tuned to approach realism or even obtain new sounds without a real world counterpart.

Finally, we hope this study could contribute to the understanding of the vibroacoustics of a piano, and to the innovation of digital musical instruments with desired characteristics of sound.

List of Figures

1	The 9 surface forces acting on the 3 positive sides of an infinitesimal volume . . .	3
2	The piano soundboard in top view (left) and side view (right)	7
3	The piano string in 3D view	8
4	The piano in a room	9
5	The piano hammer view from y (left) and x (right) direction	13
6	The piano bridge view from 3 directions	17

References

- [1] Constitutive equations. http://web.mit.edu/16.20/homepage/3_Constitutive/Constitutive_files/module_3_no_solutions.pdf. Accessed: 2024-08-06.
- [2] Stress and equations of motion. <https://www.comsol.com/multiphysics/stress-and-equations-of-motion>. Accessed: 2024-09-17.
- [3] Rolf Bader and Niko Plath. Impact of damping on oscillation patterns on the plain piano soundboard. In *Acoustics*, volume 4, pages 1013–1027. MDPI, 2022.
- [4] Balazs Bank and Juliette Chabassier. Model-based digital pianos: from physics to sound synthesis. *IEEE Signal Processing Magazine*, 36(1):103–114, 2018.
- [5] Balázs Bank and László Sujbert. Generation of longitudinal vibrations in piano strings: From physics to sound synthesis. *The Journal of the Acoustical Society of America*, 117(4):2268–2278, 2005.
- [6] Abhiram Bhanuprakash, Maarten Van Walstijn, and Vasileios Chatziioannou. Quadratic spline approximation of the contact potential for real-time simulation of lumped collisions in musical instruments. In *27th International Conference on Digital Audio Effects (DAFx24)*, pages 155–162, 2024.
- [7] Voichita Bucur. *The Acoustics of Wood (1995)*. CRC press, 2017.
- [8] Guillaume Castera and Juliette Chabassier. *Numerical analysis of quadratized schemes. Application to the simulation of the nonlinear piano string*. PhD thesis, Inria, 2023.
- [9] Guillaume Castera, Juliette Chabassier, Paul Fiset, and Brad Wagijo. *Piano bridge mobility and longitudinal precursors*. PhD thesis, Inria Bordeaux-Sud Ouest, 2023.
- [10] Juliette Chabassier, Antoine Chaigne, and Patrick Joly. Modeling and simulation of a grand piano. *The Journal of the Acoustical Society of America*, 134(1):648–665, 2013.
- [11] Juliette Chabassier, Antoine Chaigne, and Patrick Joly. Time domain simulation of a piano. part 1: model description. *ESAIM: Mathematical Modelling and Numerical Analysis*, 48(5):1241–1278, 2014.
- [12] Juliette Chabassier and Marc Duruflé. Energy based simulation of a timoshenko beam in non-forced rotation. influence of the piano hammer shank flexibility on the sound. *Journal of Sound and Vibration*, 333(26):7198–7215, 2014.
- [13] Juliette Chabassier, Marc Duruflé, and Patrick Joly. Time domain simulation of a piano. part 2: numerical aspects. *ESAIM: Mathematical Modelling and Numerical Analysis*, 50(1):93–133, 2016.
- [14] Juliette Chabassier and Sébastien Imperiale. Introduction and study of fourth order theta schemes for linear wave equations. *Journal of Computational and Applied Mathematics*, 245:194–212, 2013.
- [15] Antoine Chaigne and Jean Kergomard. *Acoustics of musical instruments*. Springer, 2016.
- [16] Michele Ducceschi and Stefan Bilbao. Simulation of the geometrically exact nonlinear string via energy quadratisation. *Journal of Sound and Vibration*, 534:117021, 2022.

- [17] Michele Ducceschi, Stefan Bilbao, Craig J Webb, et al. Real-time simulation of the struck piano string with geometrically exact nonlinearity via a scalar quadratic energy method. In *Proceedings of the ENOC 2022-10th European Nonlinear Dynamics Conference*, pages 1–8, 2022.
- [18] Michele Ducceschi, Stefan Bilbao, Silvin Willemsen, and Stefania Serafin. Linearly-implicit schemes for collisions in musical acoustics based on energy quadratisation. *The Journal of the Acoustical Society of America*, 149(5):3502–3516, 2021.
- [19] F Dunn, WM Hartmann, DM Campbell, and Neville H Fletcher. *Springer handbook of acoustics*. Springer, 2015.
- [20] Benjamin Elie, Benjamin Cotté, and Xavier Boutillon. Physically-based sound synthesis software for computer-aided-design of piano soundboards. *Acta Acustica*, 6:30, 2022.
- [21] Brian Hamilton and Stefan Bilbao. Fdtd modelling of sound propagation in air including viscothermal and relaxation effects. In *Forum Acusticum*, pages 541–543, 2020.
- [22] Brian Hamilton and Stefan Bilbao. Time-domain modeling of wave-based room acoustics including viscothermal and relaxation effects in air. *JASA Express Letters*, 1(9), 2021.
- [23] Mario Igréc. *Pianos inside out*, 2013.
- [24] Nam-Ho Kim and Nam-Ho Kim. Finite element analysis for contact problems. *Introduction to nonlinear finite element analysis*, pages 367–426, 2015.
- [25] Pablo Miranda Valiente, Giacomo Squicciarini, and David J Thompson. Influence of soundboard modelling approaches on piano string vibration. *The Journal of the Acoustical Society of America*, 155(5):3213–3232, 2024.
- [26] Philip McCord Morse and K Uno Ingard. *Theoretical acoustics*. Princeton university press, 1986.
- [27] Alan T Nettles. Basic mechanics of laminated composite plates. Technical report, 1994.
- [28] Annamaria Pau and Francesco Lanza di Scalea. Nonlinear guided wave propagation in prestressed plates. *The Journal of the Acoustical Society of America*, 137(3):1529–1540, 2015.
- [29] Jie Shen, Jie Xu, and Jiang Yang. The scalar auxiliary variable (sav) approach for gradient flows. *Journal of Computational Physics*, 353:407–416, 2018.
- [30] Jie Shen, Jie Xu, and Jiang Yang. A new class of efficient and robust energy stable schemes for gradient flows. *SIAM Review*, 61(3):474–506, 2019.
- [31] Jin Jack Tan. *Piano acoustics: string’s double polarisation and piano source identification*. PhD thesis, Université Paris Saclay (COMUE), 2017.
- [32] Jin-Jack Tan, Cyril Touzé, and Benjamin Cotté. Double polarisation in nonlinear vibrating piano strings. In *Third Vienna Talk on Music Acoustics, 2015*, 2015.
- [33] Benjamin Trévisan, Kerem Ege, and Bernard Laulagnet. A modal approach to piano soundboard vibroacoustic behavior. *The Journal of the Acoustical Society of America*, 141(2):690–709, 2017.
- [34] Pablo Miranda Valiente, Giacomo Squicciarini, and David Thompson. Modeling the interaction between piano strings and the soundboard. In *Proceedings of Meetings on Acoustics*, volume 49. AIP Publishing, 2022.
- [35] Maarten Van Walstijn, Abhiram Bhanuprakash, and Paul Stapleton. Finite-difference simulation of linear plate vibration with dynamic distributed contact. In *Sound and Music Computing Conference 2021*, pages 92–99, 2021.
- [36] Maarten Van Walstijn, Vasileios Chatziioannou, and Abhiram Bhanuprakash. Implicit and explicit schemes for energy-stable simulation of string vibrations with collisions: Refinement, analysis, and comparison. *Journal of Sound and Vibration*, 569:117968, 2024.

- [37] Peter Wriggers. Finite element algorithms for contact problems. *Archives of computational methods in engineering*, 2:1–49, 1995.
- [38] Jia Zhao, Qi Wang, and Xiaofeng Yang. Numerical approximations for a phase field dendritic crystal growth model based on the invariant energy quadratization approach. *International Journal for Numerical Methods in Engineering*, 110(3):279–300, 2017.

A Prestrain and prestress

Consider 3 configurations of a material: natural \rightarrow initial \rightarrow current [28]. In the natural configuration, no prestrain and prestress is present. In the initial configuration, prestrain and prestress exist. In the current configuration, strain and stress emerge in addition to prestrain and prestress. Under the same xyz coordinate system, define \mathbb{R}^3 vectors $\bar{\mathbf{x}}, \mathbf{x}, \hat{\mathbf{x}}$ as the coordinates of the same material particle in the natural, initial and current configurations respectively. The following relation holds:

$$\begin{aligned}\mathbf{x} &= \bar{\mathbf{x}} + \bar{\mathbf{u}}(\bar{\mathbf{x}}), \\ \hat{\mathbf{x}} &= \mathbf{x} + \mathbf{u}(\mathbf{x}),\end{aligned}\tag{A.1}$$

where $\bar{\mathbf{u}}$ and \mathbf{u} are the displacement vectors from natural to initial and from initial to current configurations respectively. Denote deformation gradients $\hat{\mathbf{Z}} = \frac{\partial \hat{\mathbf{x}}}{\partial \bar{\mathbf{x}}}$, $\mathbf{Z} = \frac{\partial \mathbf{x}}{\partial \bar{\mathbf{x}}}$ and $\bar{\mathbf{Z}} = \frac{\partial \mathbf{x}}{\partial \hat{\mathbf{x}}}$; denote Jacobian matrices $\mathbf{J} = \nabla \mathbf{u}$, $\bar{\mathbf{J}} = \nabla \bar{\mathbf{u}}$. We then have

$$\begin{aligned}\mathbf{Z} &= \mathbf{I} + \mathbf{J}, \quad \bar{\mathbf{Z}} = \mathbf{I} + \bar{\mathbf{J}}, \\ \hat{\mathbf{Z}} &= \mathbf{Z}\bar{\mathbf{Z}} = (\mathbf{I} + \mathbf{J})(\mathbf{I} + \bar{\mathbf{J}}).\end{aligned}\tag{A.2}$$

The Green-Lagrange strain tensor of current configuration with respect to natural configuration is

$$\begin{aligned}\hat{\mathbf{E}} &= \frac{1}{2} \left(\hat{\mathbf{Z}}^\top \hat{\mathbf{Z}} - \mathbf{I} \right) = (\mathbf{I} + \bar{\mathbf{J}})^\top (\mathbf{I} + \mathbf{J})^\top (\mathbf{I} + \mathbf{J})(\mathbf{I} + \bar{\mathbf{J}}) \\ &= \frac{1}{2} \left(\bar{\mathbf{J}} + \bar{\mathbf{J}}^\top + \bar{\mathbf{J}}^\top \bar{\mathbf{J}} \right) + \frac{1}{2} \left(\mathbf{I} + \bar{\mathbf{J}}^\top \right) \left(\mathbf{J} + \mathbf{J}^\top + \mathbf{J}^\top \mathbf{J} \right) (\mathbf{I} + \bar{\mathbf{J}}) \\ &\approx \bar{\mathbf{E}} = \boldsymbol{\epsilon} + \bar{\mathbf{E}} + \left(\bar{\mathbf{J}}^\top \boldsymbol{\epsilon} + \boldsymbol{\epsilon} \bar{\mathbf{J}} + \bar{\mathbf{J}}^\top \boldsymbol{\epsilon} \bar{\mathbf{J}} \right),\end{aligned}\tag{A.3}$$

where $\bar{\mathbf{E}} = \frac{1}{2} \left(\bar{\mathbf{J}} + \bar{\mathbf{J}}^\top + \bar{\mathbf{J}}^\top \bar{\mathbf{J}} \right)$ is the prestrain tensor, and $\boldsymbol{\epsilon} = \frac{1}{2} \left(\mathbf{J} + \mathbf{J}^\top \right)$ is the engineering strain discarding the second-order $\frac{1}{2} \mathbf{J}^\top \mathbf{J}$ term for the sake of linearization. Note this linearization should . Assuming $\bar{\mathbf{J}} = \{\bar{J}_{ij}\}$ is symmetric, viz. no rigid body rotation, then we have eigen decomposition $\bar{\mathbf{J}} = \mathbf{U} \text{diag}(\lambda_1, \lambda_2, \lambda_3) \mathbf{U}^\top$ and

$$\begin{aligned}\bar{\mathbf{J}} + \frac{1}{2} \bar{\mathbf{J}}^2 &= \bar{\mathbf{E}} \\ \mathbf{U} \begin{bmatrix} \lambda_1 + \frac{1}{2} \lambda_1^2 & & \\ & \lambda_2 + \frac{1}{2} \lambda_2^2 & \\ & & \lambda_3 + \frac{1}{2} \lambda_3^2 \end{bmatrix} \mathbf{U}^\top &= \mathbf{U} \begin{bmatrix} \lambda'_1 & & \\ & \lambda'_2 & \\ & & \lambda'_3 \end{bmatrix} \mathbf{U}^\top,\end{aligned}\tag{A.4}$$

from which $\lambda_i = 4\sqrt{\lambda'_i + 4} - 8$ is the solution and $\bar{\mathbf{J}}$ can be computed per eigen decomposition. The uniqueness of this solution stems from that the principal stretches $\lambda'_i \geq -1$ should hold for normal cases, viz. no negative compression, and λ_i should be close to λ'_i to be consistent with the case of ignoring $\frac{1}{2} \bar{\mathbf{J}}^2$. If the prestrain is not large enough to induce non-negligible geometric nonlinearity, $\frac{1}{2} \bar{\mathbf{J}}^\top \bar{\mathbf{J}}$ can be disregarded and $\bar{\mathbf{J}} = \bar{\mathbf{E}}$ simply holds. But generally for string instruments like piano, prestrain may be large and even dominate the post-strain, thus we should cover the geometric nonlinearity of prestrain. This, however, would not necessarily make (A.3) nonlinear with respect to \mathbf{J} , because strain deformation is normally small enough to make $\frac{1}{2} \mathbf{J}^\top \mathbf{J}$ negligible. Consequently, with $\bar{\mathbf{J}}$ and $\bar{\mathbf{E}}$ known, the prestrain model (A.3) is reasonably

linear with respect to the unknowns. Converting it into vector form, we find

$$\begin{aligned} \vec{\mathbf{E}} \approx \vec{\mathbf{E}} = \vec{\mathbf{E}} + \vec{\mathbf{E}}_{\text{dyn}}, \quad \vec{\mathbf{E}}_{\text{dyn}} = (\mathbf{I} + \Psi_2 \Psi_1) \vec{\boldsymbol{\epsilon}}, \quad \Psi_1 = \begin{bmatrix} 2 & 0 & 0 & 0 & 0 & 0 \\ 0 & 2 & 0 & 0 & 0 & 0 \\ 0 & 0 & 2 & 0 & 0 & 0 \\ 0 & 0 & 0 & 1 & 0 & 0 \\ 0 & 0 & 0 & 0 & 1 & 0 \\ 0 & 0 & 0 & 0 & 0 & 1 \end{bmatrix} \\ \Psi_2 = \begin{bmatrix} \bar{J}_{11}(\bar{J}_{11}+2) & \bar{J}_{12}^2 & \bar{J}_{13}^2 & \bar{J}_{12}(\bar{J}_{11}+1) & \bar{J}_{13}(\bar{J}_{11}+1) & \bar{J}_{12}\bar{J}_{13} \\ & \bar{J}_{22}(\bar{J}_{22}+2) & \bar{J}_{23}^2 & \bar{J}_{12}(\bar{J}_{22}+1) & \bar{J}_{12}\bar{J}_{23} & \bar{J}_{23}(\bar{J}_{22}+1) \\ & & \bar{J}_{33}(\bar{J}_{33}+2) & \bar{J}_{13}\bar{J}_{23} & \bar{J}_{13}(\bar{J}_{33}+1) & \bar{J}_{23}(\bar{J}_{33}+1) \\ & & & \bar{J}_{11}\bar{J}_{22} + \bar{J}_{11} + \bar{J}_{12}^2 + \bar{J}_{22} & \bar{J}_{11}\bar{J}_{23} + \bar{J}_{12}\bar{J}_{13} + \bar{J}_{23} & \bar{J}_{12}\bar{J}_{23} + \bar{J}_{13}\bar{J}_{22} + \bar{J}_{13} \\ \text{Sym} & & & & \bar{J}_{11}\bar{J}_{33} + \bar{J}_{11} + \bar{J}_{13}^2 + \bar{J}_{33} & \bar{J}_{12}\bar{J}_{33} + \bar{J}_{12} + \bar{J}_{13}\bar{J}_{23} \\ & & & & & \bar{J}_{22}\bar{J}_{33} + \bar{J}_{22} + \bar{J}_{23}^2 + \bar{J}_{33} \end{bmatrix} \end{aligned} \quad (\text{A.5})$$

where $\vec{\mathbf{E}}_{\text{dyn}}$ is the dynamic part of strain vector; all the vectors here are defined similar to (2.3). It is now straight forward that the prestrain functions a linear transformation (addition and scaling) of the strain at a first approximation. However, as in (A.5) $\bar{E}_{ij}(\bar{\mathbf{x}})$ is expressed in natural coordinates, converting it into initial coordinate representations to align with $\vec{\boldsymbol{\epsilon}}$ would be preferable. In order for this, define prestress vector $\vec{\mathbf{S}}(\bar{\mathbf{x}})$, then $\vec{\mathbf{E}} = \mathbf{D}^{-1} \vec{\mathbf{S}}$. From (A.1), an inverse mapping $\bar{\mathbf{x}} = f(\mathbf{x})$ should exist. If we let $\vec{\mathbf{T}}(\mathbf{x}) = \vec{\mathbf{S}}(f(\mathbf{x}))$, the vectorized tension field from (2.8), and substitute $\vec{\mathbf{E}} = \mathbf{D}^{-1} \vec{\mathbf{T}}(\mathbf{x})$ into (A.4)(A.5), then the total strain $\hat{\mathbf{E}}$ can be expressed in only the initial configurations. The advantage of this is not only avoiding finding the intricate natural coordinates, but also making it straightforward to satisfy static equilibrium by condition $\nabla \cdot \mathbf{T}(\mathbf{x}) = \mathbf{0}$.

Given the strain vector $\vec{\mathbf{E}}$, the dynamic strain energy is

$$\begin{aligned} U &= \int_{\Omega} \int_{\mathbf{0}}^{\vec{\mathbf{E}}_{\text{dyn}}} \Psi_0 \vec{\mathbf{S}}_{\text{dyn}} \cdot d\vec{\mathbf{E}}_{\text{dyn}} dV \\ &= \int_{\Omega} \int_{\mathbf{0}}^{\vec{\mathbf{E}}_{\text{dyn}}} \Psi_0 \mathbf{D} \vec{\mathbf{E}}_{\text{dyn}} \cdot d\vec{\mathbf{E}}_{\text{dyn}} dV \\ &= \frac{1}{2} \int_{\Omega} \Psi_0 \vec{\mathbf{E}}_{\text{dyn}} \cdot \mathbf{D} \vec{\mathbf{E}}_{\text{dyn}} dV \\ &= \int_{\Omega} \frac{1}{2} \Psi_0 \vec{\boldsymbol{\epsilon}} \cdot \left(\mathbf{D} + \Psi_1^{\top} \Psi_2^{\top} \mathbf{D} \Psi_2 \Psi_1 \right) \vec{\boldsymbol{\epsilon}} dV, \end{aligned} \quad (\text{A.6})$$

where $\Psi_0(\mathbf{x}) = \det(\bar{\mathbf{Z}})^{-1}$ is the volume factor linear w.r.t. the unknowns, accounts for volume change from natural to current configuration, and can be computed given $\bar{\mathbf{J}}$. Note that $\vec{\mathbf{S}}_{\text{dyn}}$ here is understood as the (dynamic) second Piola-Kirchhoff (PK2) stress that is energy conjugate to $\vec{\mathbf{E}}_{\text{dyn}}$. Though PK2 should be formulated in the natural configuration, we have transformed it to the initial configuration along with the volume factor. According to [2], PK2 may also be changed to Cauchy stress in the initial configuration, but it is unnecessary here because the strain energy is the same even without doing so. And anyway, what we seek for here is not PK2, but the dynamic stress vector $\vec{\boldsymbol{\sigma}}$ that is energy conjugate to $\vec{\boldsymbol{\epsilon}}$, which can be derived from the expression of dynamic strain energy as

$$\vec{\boldsymbol{\sigma}} = (\mathbf{D} \vec{\boldsymbol{\epsilon}} + \vec{\boldsymbol{\tau}}), \quad \vec{\boldsymbol{\tau}} + \Psi_0 \Psi_1^{\top} \Psi_2^{\top} \mathbf{D} \Psi_2 \Psi_1 \vec{\boldsymbol{\epsilon}}, \quad (\text{A.7})$$

where $\vec{\boldsymbol{\tau}}$ is the dynamic prestress vector. It is now clear that the effect of prestress can be seen as adding a symmetrically transformed constitutive matrix $\Psi_1^{\top} \Psi_2^{\top} \mathbf{D} \Psi_2 \Psi_1$.

Finally, we acknowledge that in the presence of large deformations from initial to current configuration, the quadratic term in the Green-Lagrange strain should be retained, leading to nonlinear operators on the unknowns for the strain energy, as well as PDEs and ODEs. However, this concern is irrelevant in case of large deformations from natural to initial configuration because even if prestrain itself is nonlinear, it is linear w.r.t. the strain where the unknowns are contained

in. Another more intricate nonlinearity, often known as the geometric nonlinearity, arises if we want to express stress and prestress in the current configuration. This would require transforming PK2 to Cauchy stress, yet we have not encountered the necessity for doing so in the present context.

B Lagrangian formulation

As a complement to the Newtonian formulation, we present a non-conservative Lagrangian formulation of the 3D elastic material model. To derive system ODEs (weak form) in a more straightforward way, FEM space discretization is incorporated into the Lagrangian formulation, skipping the intermediate PDEs (strong form). As per (2.17), the kinetic energy and its variation over $[t_0, t_1]$ are

$$\begin{aligned} E_k &= \int_{\Omega} \frac{1}{2} \rho \dot{\mathbf{u}} \cdot \dot{\mathbf{u}} dV = \frac{1}{2} \int_{\Omega} \dot{\boldsymbol{\xi}} \cdot \rho \mathbf{P}^{\top} \mathbf{P} \dot{\boldsymbol{\xi}} dV \\ \int_{t_0}^{t_1} \delta E_k dt &= \int_{t_0}^{t_1} \int_{\Omega} \delta \dot{\boldsymbol{\xi}} \cdot \rho \mathbf{P}^{\top} \mathbf{P} \dot{\boldsymbol{\xi}} dV dt = - \int_{t_0}^{t_1} \int_{\Omega} \delta \boldsymbol{\xi} \cdot \rho \mathbf{P}^{\top} \mathbf{P} \ddot{\boldsymbol{\xi}} dV dt \end{aligned} \quad (\text{B.1})$$

where integration by parts is utilized assuming

$$\delta \boldsymbol{\xi}(t_0) = \delta \boldsymbol{\xi}(t_1) = \mathbf{0}. \quad (\text{B.2})$$

Note that we have excluded $\boldsymbol{\xi}_0$ in the derivation of kinetic energy because nonzero $\boldsymbol{\xi}_0$ (boundary displacements) actually implies the existence some non-conservative forces (e.g. constraints). Nevertheless, we can compute the ‘‘virtual kinetic energy’’ as

$$\int_{t_0}^{t_1} \delta E_{k,0} = \int_{t_0}^{t_1} \int_{\Omega} \delta \dot{\boldsymbol{\xi}} \cdot \rho \mathbf{P}^{\top} \mathbf{P}_0 \dot{\boldsymbol{\xi}}_0 dV dt \quad (\text{B.3})$$

The potential energy and its variation are

$$\begin{aligned} E_p &= - \int_{\Omega} \frac{1}{2} \mathbf{u} \cdot \text{Div}(\boldsymbol{\sigma} + \boldsymbol{\tau}) dV \\ &= - \int_{\Gamma} \left(\frac{1}{2} \sum_{i=1}^3 u_i (\boldsymbol{\sigma}_i + \boldsymbol{\tau}_i) \right) \cdot d\Gamma + \int_{\Omega} \left(\frac{1}{2} \sum_{i=1}^3 \nabla u_i \cdot (\boldsymbol{\sigma}_i + \boldsymbol{\tau}_i) \right) dV \\ &= \int_{\Omega} \left[\sum_{i=1}^3 \frac{1}{2} (\boldsymbol{\xi} \cdot \mathbf{Q}_i^{\top} (\mathbf{A}_i + \mathbf{B}_i) \mathbf{Q} \boldsymbol{\xi}) \right] dV \\ &= \int_{\Omega} \frac{1}{2} \boldsymbol{\xi} \cdot \mathbf{Q}^{\top} (\mathbf{A} + \mathbf{B}) \mathbf{Q} \boldsymbol{\xi} dV \\ \delta E_p &= \int_{\Omega} \delta \boldsymbol{\xi} \cdot \mathbf{Q}^{\top} (\mathbf{A} + \mathbf{B}) \mathbf{Q} \boldsymbol{\xi} dV \end{aligned} \quad (\text{B.4})$$

where Dirichlet or Neumann boundary conditions should automatically apply to ensure the integral on the boundary is zero. Similar to the kinetic energy, nonzero $\boldsymbol{\xi}_0$ does not correspond to a potential energy but a ‘‘virtual potential energy’’ (equivalent to virtual work but sign flipped here for convenience) as

$$\delta E_{p,0} = \int_{\Omega} \delta \boldsymbol{\xi} \cdot \mathbf{Q}^{\top} (\mathbf{A} + \mathbf{B}) \mathbf{Q}_0 \boldsymbol{\xi}_0 dV \quad (\text{B.5})$$

As for the damping force which is non-conservative, we can compute its virtual work as

$$\begin{aligned} \delta W_d &= 2\mu \int_{\Omega} \delta \mathbf{u} \cdot \text{Div}(\dot{\boldsymbol{\sigma}} + \dot{\boldsymbol{\tau}}) dV \\ &= -2\mu \int_{\Omega} \left[\sum_{i=1}^3 \delta \nabla u_i \cdot (\dot{\boldsymbol{\sigma}}_i + \dot{\boldsymbol{\tau}}_i) \right] dV \\ &= -2\mu \int_{\Omega} \delta \boldsymbol{\xi} \cdot \left[\mathbf{Q}^{\top} (\mathbf{A} + \mathbf{B}) \mathbf{Q} \dot{\boldsymbol{\xi}} + \mathbf{Q}^{\top} (\mathbf{A} + \mathbf{B}) \mathbf{Q}_0 \dot{\boldsymbol{\xi}}_0 \right] dV. \end{aligned} \quad (\text{B.6})$$

It can be verified that the virtual work approach is also applicable to conservative forces like stress and prestress to derive the identical potential energy functions. For other non-conservative forces, the virtual work is

$$\delta W_{nc} = \int_{\Omega} \delta \mathbf{u} \cdot \mathbf{F} dV = \int_{\Omega} \delta \boldsymbol{\xi} \cdot \mathbf{P}^{\top} \mathbf{F} dV. \quad (\text{B.7})$$

Applying the principle of virtual work, we derive the energy equation

$$\int_{t_0}^{t_1} (\delta E_k + \delta E_{k,0} - \delta E_p - \delta E_{p,0} + \delta W_d + \delta W_{nc}) dt = - \int_{t_0}^{t_1} \delta \boldsymbol{\xi} \cdot (\mathbf{M} \ddot{\boldsymbol{\xi}} + \mathbf{C} \dot{\boldsymbol{\xi}} + \mathbf{K} \boldsymbol{\xi} - \mathbf{f}) dt = 0, \quad (\text{B.8})$$

where \mathbf{M} , \mathbf{C} , \mathbf{K} , \mathbf{f} are defined in (2.20). Since $\delta \boldsymbol{\xi}$ is arbitrary as long as (B.2) is satisfied, (2.19) can be derived from (B.8).

C Elastic material contacting rigid surface in 3D setting

We now consider the case of a material A contacting another material B in a fully 3D setting, where A is elastic with weak form ODEs like (2.19) and B's contact surface is rigid (hence B may still be an elastic material). In this case, applying Dirichlet boundary conditions through $\boldsymbol{\xi}_0(t)$ would be infeasible because not only the contact status (in contact or not) but also the contact boundary changes with time. As we shall see, the potential contact boundary is Dirichlet when contact is present meaning that boundary stress and strain appear, and is Neumann when contact is absent meaning that boundary stress and strain vanish. This leads to a time-varying dimension (number of DOFs) of the system ODEs, invalidating the modal superposition method. To model the dynamic evolution of contact system, we adopt the master-slave idea and will brief describe our understanding and application of it. Readers can refer to [37][24] for a comprehensive and rigorous FEM formulation of the contact problem.

Consider a system of second-order ODEs where the rhs source term depends on the DOFs:

$$\mathbf{M} \ddot{\boldsymbol{\xi}}(t) + \mathbf{C} \dot{\boldsymbol{\xi}}(t) + \mathbf{K} \boldsymbol{\xi}(t) = \mathbf{f}(t), \quad \mathbf{f}(t) = \mathbf{r}(t, \boldsymbol{\xi}(t), \dot{\boldsymbol{\xi}}(t)). \quad (\text{C.1})$$

To derive time stepping algorithms like those in 7.2, we first integrate (C.1) over $[t_n, t_{n+1}]$ to yield

$$\begin{aligned} \mathbf{M} [\dot{\boldsymbol{\xi}}(t_{n+1}) - \dot{\boldsymbol{\xi}}(t_n)] &= -\mathbf{C} [\boldsymbol{\xi}(t_{n+1}) - \boldsymbol{\xi}(t_n)] - \mathbf{K} \int_{t_n}^{t_{n+1}} \boldsymbol{\xi}(t) dt + \int_{t_n}^{t_{n+1}} \mathbf{f}(t) dt \\ \mathbf{M} [\dot{\boldsymbol{\xi}}(t_{n+1}) - \dot{\boldsymbol{\xi}}(t_n)] &\approx -\mathbf{C} [\boldsymbol{\xi}(t_{n+1}) - \boldsymbol{\xi}(t_n)] - \frac{h}{2} \mathbf{K} [\boldsymbol{\xi}(t_n) + \boldsymbol{\xi}(t_{n+1})] + h \mathbf{f}(t_n) + \frac{h^2}{2} \dot{\mathbf{f}}(t_n). \end{aligned} \quad (\text{C.2})$$

Combining this with

$$\boldsymbol{\xi}(t_{n+1}) - \boldsymbol{\xi}(t_n) = \int_{t_n}^{t_{n+1}} \dot{\boldsymbol{\xi}}(t) dt \approx \frac{h}{2} [\dot{\boldsymbol{\xi}}(t_n) + \dot{\boldsymbol{\xi}}(t_{n+1})], \quad (\text{C.3})$$

the update scheme for DOFs vector is found to be

$$\begin{aligned} \boldsymbol{\xi}(t_{n+1}) &= \mathbf{Z}_1^{-1} \left[\mathbf{Z}_0 \boldsymbol{\xi}(t_n) + 2\mathbf{M} \dot{\boldsymbol{\xi}}(t_n) + h \mathbf{f}(t_n) + \frac{h^2}{2} \dot{\mathbf{f}}(t_n) \right], \\ \dot{\boldsymbol{\xi}}(t_{n+1}) &= \frac{2}{h} \boldsymbol{\xi}(t_{n+1}) - \frac{2}{h} \boldsymbol{\xi}(t_n) - \dot{\boldsymbol{\xi}}(t_n), \end{aligned} \quad (\text{C.4})$$

where

$$\begin{aligned} \mathbf{Z}_0 &= \frac{2}{h} \mathbf{M} + \mathbf{C} - \frac{h}{2} \mathbf{K}, \\ \mathbf{Z}_1 &= \frac{2}{h} \mathbf{M} + \mathbf{C} + \frac{h}{2} \mathbf{K}. \end{aligned} \quad (\text{C.5})$$

It now suffices to describe the time stepping algorithm for contact problem as follows:

1. At time step t_n , set iteration steps $j = 1$ and $j_{\max} > 1$; set $\xi_j^a(t_n) = \xi_j(t_n) = \xi(t_n)$, $\dot{\xi}_j^a(t_n) = \dot{\xi}_j(t_n) = \dot{\xi}(t_n)$, $f_j^a(t_n) = f_j^a(t_n) = \mathbf{0}$, $M_j^a = M$, $C_j^a = C$, $K_j^a = K$. Here we assume the rhs source only comes from contact between A and B. If any other rhs sources are present and independent of this contact, add them to $f_j^a(t_n)$ and $\dot{f}_j^a(t_n)$.
2. Input $\xi_j^a(t_n)$, $\dot{\xi}_j^a(t_n)$, $f_j^a(t_n)$, $\dot{f}_j^a(t_n)$, M_j^a , C_j^a , K_j^a into (C.4) to compute $\xi_j^a(t_{n+1})$ and $\dot{\xi}_j^a(t_{n+1})$.
3. Based on $\xi_j^a(t_{n+1})$ and $\dot{\xi}_j^a(t_{n+1})$, check if A “penetrates” B at any potential contact boundary nodes using a geometry searching algorithm. Here $\xi_j^a(t_{n+1})$ and $\dot{\xi}_j^a(t_{n+1})$ are used to compute A’s surface forces acting on B, so as to obtain B’s displacements at t_{n+1} .
 - (a) If penetration occurs at some nodes:
 - i. Set $j \leftarrow j + 1$.
 - A. If $j > j_{\max}$, go to step 4.
 - B. Otherwise, reclassify $\xi_j(t_n)$, $\dot{\xi}_j(t_n)$ (all DOFs, dimension N) into $\xi_j^a(t_n)$, $\dot{\xi}_j^a(t_n)$ (non-penetrated DOFs, dimension N_j^a and $\xi_j^b(t_n)$, $\dot{\xi}_j^b(t_n)$ (penetrated DOFs, dimension N_j^b). Note here $\xi_{j-1}^b(t_n)$, $\dot{\xi}_{j-1}^b(t_n)$ (if any) must be classified as penetrated in $\xi_j^b(t_n)$, $\dot{\xi}_j^b(t_n)$. Accordingly, M , C , K are adjusted to M_j^a , C_j^a , K_j^a with dimension N_j^a , in a way as if ξ_j^a were ξ (unknown DOFs) and ξ_j^b were ξ_0 (known DOFs) in (2.20). Using $\xi_j^b(t_n)$ and $\dot{\xi}_j^b(t_n)$ (Dirichlet boundary conditions), $f_j^a(t_n)$ and $\dot{f}_j^a(t_n)$ with dimension N_j^a can be computed.
 - ii. Input $\xi_j^a(t_n)$, $\dot{\xi}_j^a(t_n)$, $f_j^a(t_n)$, $\dot{f}_j^a(t_n)$, M_j^a , C_j^a , K_j^a into (C.4) to compute $\xi_j^a(t_{n+1})$ and $\dot{\xi}_j^a(t_{n+1})$.
 - iii. Based on $\xi_j^a(t_{n+1})$ and $\dot{\xi}_j^a(t_{n+1})$, check if A “penetrates” B at any potential contact boundary nodes using a geometry searching algorithm. Here $\xi_j^a(t_{n+1})$ and $\dot{\xi}_j^a(t_{n+1})$ are used to compute A’s surface forces acting on B, so as to obtain B’s displacements at t_{n+1} , as well as $\xi_j^b(t_{n+1})$ and $\dot{\xi}_j^b(t_{n+1})$. Note here if $\xi_j^b(t_{n+1})$ is not well-defined due to non-smoothness, the weak derivative may be adopted as an alternative. Combine $\xi_j^a(t_{n+1})$, $\dot{\xi}_j^a(t_{n+1})$ and $\xi_j^b(t_{n+1})$, $\dot{\xi}_j^b(t_{n+1})$ to get $\xi_j(t_{n+1})$ and $\dot{\xi}_j(t_{n+1})$.
 - A. If penetration occurs at some nodes, go back to step 3.(a).i.
 - B. Otherwise, go to step 4.
 - (b) Otherwise, set $\xi_j(t_{n+1}) = \xi_j^a(t_{n+1})$, $\dot{\xi}_j(t_{n+1}) = \dot{\xi}_j^a(t_{n+1})$.
4. End the current time step with $\xi(t_{n+1}) = \xi_j(t_{n+1})$ and $\dot{\xi}(t_{n+1}) = \dot{\xi}_j(t_{n+1})$, and move on to the next time step.

The basic idea of this algorithm is to try Neumann first, and if penetration occurs then change to Dirichlet. This strategy can be justified from an energy perspective: first seek for displacements minimizing the Lagrangian and virtual work of the system without any constraint; if unrealistic penetration occurs, add an equality constraint regarding Dirichlet boundary displacements, so as to find displacements minimizing the Lagrangian and virtual work under contact constraint (similar to the Lagrange multipliers). This check of penetration can lead to the nonlinearity and non-smoothness of a contact problem. For geometry searching algorithms needed to check penetration, we refer to the [COMSOL description]. If the contact boundary is assumed to be only a fixed point, then only one or two iterations per time step is needed.

Certain contact problems may involve deformations large enough to induce non-negligible nonlinearity. For nonlinearity of strain, the Green-Lagrange strain instead of the engineering strain may be needed. For nonlinearity of stress, the second-Piola–Kirchhoff stress tensor instead of the Cauchy stress tensor may be needed. This would introduce another kind of nonlinearity into the contact model. While the nonlinearity due to contact’s one-sided nature still keeps the computation of each iteration in one time step linear, the nonlinearity due to nonlinear stress and strain can make the PDEs as well as ODEs nonlinear, meaning that computation of each

iteration is nonlinear if no linearization is applied. If the nonlinear perturbation to the equations is small (controlled by some “small parameters”), the perturbation method applying linearization several times is acceptable; otherwise, the perturbation method would suffer significant accuracy loss.

D An energy-stable scheme for nonlinear forces

To better solve elastic solid problems subject to deformation nonlinearity, particularly elastic contact and piano string vibration, we are working on integrating into our model the invariant energy quadratization (IEQ) method [38] and scalar auxiliary variable (SAV) method [29, 30]. Based on the idea of IEQ, SAV is a recent advancement in computational physics towards efficient and energy-stable time discretization scheme for gradient flows. Both methods have been applied to musical instruments modeling, achieving discrete energy evolution (conservation or dissipation) that is consistent with the continuous counterpart, using fully explicit or linearly implicit update schemes [18, 36, 6]. These schemes attain the desired discrete energy-stable property while being more efficient than existing nonlinear solvers many of which rely on Newton-Raphson like iterations with computationally expensive Jacobian matrices.

To introduce nonlinearity into the 3D elastic solid model, we rewrite (2.19) as

$$M\ddot{\boldsymbol{\xi}}(t) + C\dot{\boldsymbol{\xi}}(t) + K\boldsymbol{\xi}(t) + \mathbf{g}[\boldsymbol{\xi}(t)] = \mathbf{f}(t), \quad (\text{D.1})$$

where $\mathbf{g}(\boldsymbol{\xi})$ is an operator incorporating all the “symmetric” nonlinear forces of the system, which can be conservative or non-conservative. The symmetry property we require here means that \mathbf{g} is a self-adjoint operator thus the variational Jacobian matrix

$$\mathbf{J}[\boldsymbol{\xi}(t)] = \delta_{\boldsymbol{\xi}}\mathbf{g} \quad (\text{D.2})$$

is symmetric. This is equivalent to \mathbf{g} being a self-adjoint operator. For simplicity we have not considered nonlinear damping forces in the form of $\mathbf{g}_1(\dot{\boldsymbol{\xi}})$ here, but they can simply be treated in a similar way to $\mathbf{g}(\boldsymbol{\xi})$. An example of nonlinear symmetric forces is the nonlinear stress arising from the quadratic term in Green-Lagrange strain, as well as the damping force proportional to its first-order time derivative. Anyway, linear or nonlinear forces not satisfying this symmetry property are incorporated in $\mathbf{f}(t)$, and unfortunately the coupling forces in our piano model are probably such examples. The symmetry property has important implications that one can define a nonlinear energy functional as

$$E_{nl}[\boldsymbol{\xi}(t)] = \int_0^t \dot{\boldsymbol{\xi}}(t') \cdot \mathbf{g}[\boldsymbol{\xi}(t')] dt', \quad (\text{D.3})$$

with first-order time derivative

$$\partial_t E_{nl}[\boldsymbol{\xi}(t)] = \dot{\boldsymbol{\xi}}(t) \cdot \mathbf{g}[\boldsymbol{\xi}(t)], \quad (\text{D.4})$$

and variation

$$\begin{aligned} \delta E_{nl}[\boldsymbol{\xi}(t)] &= \int_0^t \delta \dot{\boldsymbol{\xi}} \cdot \mathbf{g} dt' + \int_0^t \dot{\boldsymbol{\xi}} \cdot \delta \mathbf{g} dt', \\ &= \delta \boldsymbol{\xi}(t) \cdot \mathbf{g} - \delta \boldsymbol{\xi}(0) \cdot \mathbf{g} + \int_0^t \dot{\boldsymbol{\xi}} \cdot \delta \mathbf{g} dt' - \int_0^t \delta \boldsymbol{\xi} \cdot \dot{\mathbf{g}} dt' \\ &= \delta \boldsymbol{\xi}(t) \cdot \mathbf{g} \end{aligned} \quad (\text{D.5})$$

where $\delta \boldsymbol{\xi}(0) = \mathbf{0}$ is imposed and one can derive $\dot{\boldsymbol{\xi}} \cdot \delta \mathbf{g} - \delta \boldsymbol{\xi} \cdot \dot{\mathbf{g}} = \mathbf{0}$ with the symmetry property of \mathbf{J} . It is now clear that under symmetry, the virtual work equates real work. The kinetic energy functional is

$$\begin{aligned} E_k[\boldsymbol{\xi}(t)] &= \frac{1}{2} \dot{\boldsymbol{\xi}}(t) \cdot M \dot{\boldsymbol{\xi}}(t), \\ \partial_t E_k[\boldsymbol{\xi}(t)] &= \dot{\boldsymbol{\xi}}(t) \cdot M \ddot{\boldsymbol{\xi}}(t). \end{aligned} \quad (\text{D.6})$$

The linear potential energy functional is

$$\begin{aligned} E_p [\boldsymbol{\xi}(t)] &= \frac{1}{2} \boldsymbol{\xi}(t) \cdot \mathbf{K} \boldsymbol{\xi}(t), \\ \partial_t E_p [\boldsymbol{\xi}(t)] &= \dot{\boldsymbol{\xi}}(t) \cdot \mathbf{K} \boldsymbol{\xi}(t). \end{aligned} \quad (\text{D.7})$$

The overall energy evolution of the system is found to be

$$\begin{aligned} \dot{\boldsymbol{\xi}}(t) \cdot \left(\mathbf{M} \ddot{\boldsymbol{\xi}}(t) + \mathbf{C} \dot{\boldsymbol{\xi}}(t) + \mathbf{K} \boldsymbol{\xi}(t) + \mathbf{g} [\boldsymbol{\xi}(t)] \right) &= \dot{\boldsymbol{\xi}}(t) \cdot \mathbf{f}(t) \\ \partial_t E &= \partial_t E_k + \partial_t E_p + \partial_t E_{nl} = \dot{\boldsymbol{\xi}}(t) \cdot \mathbf{f}(t) - \dot{\boldsymbol{\xi}}(t) \cdot \mathbf{C} \dot{\boldsymbol{\xi}}(t) \end{aligned} \quad (\text{D.8})$$

where $E[\boldsymbol{\xi}(t)] = E_k + E_p + E_{nl}$.

To apply SAV [29], assume the nonlinear potential energy functional can be rewritten in the square of a scalar variable $\psi(t)$ as

$$E_{nl} [\boldsymbol{\xi}(t)] = \frac{1}{2} \psi(t)^2, \quad (\text{D.9})$$

where

$$\psi(t) = \sqrt{2} \sqrt{E_{nl} [\boldsymbol{\xi}(t)] + C_0}, \quad (\text{D.10})$$

$$\dot{\psi}(t) = \frac{1}{\sqrt{2}} \frac{\dot{\boldsymbol{\xi}}(t) \cdot \mathbf{g} [a(t), \boldsymbol{\xi}(t), \dot{\boldsymbol{\xi}}(t)]}{\sqrt{E_{nl} [\boldsymbol{\xi}(t)] + C_0}}, \quad (\text{D.11})$$

and $E_{nl} [\boldsymbol{\xi}(t)] \geq -C_0$ is assumed (bounded from below). Utilizing the Crank–Nicolson scheme described in [30] we have

$$\begin{aligned} \int_{t_n}^{t_{n+1}} \mathbf{g} dt &= \frac{1}{\sqrt{2}} \int_{t_n}^{t_{n+1}} \frac{\psi(t)}{\sqrt{E_{nl} [\boldsymbol{\xi}(t)]}} \mathbf{g} [\boldsymbol{\xi}(t)] dt \\ &\approx \frac{h}{2\sqrt{2}} \frac{\psi(t_n) + \psi(t_{n+1})}{\sqrt{E_{nl} [\boldsymbol{\xi}(t_{n+\frac{1}{2}})]} + C_0} \mathbf{g} [\boldsymbol{\xi}(t_{n+\frac{1}{2}})] \\ &\approx \frac{h}{2\sqrt{2}} \frac{\psi(t_n) + \psi(t_{n+1})}{\sqrt{E_{nl} [\boldsymbol{\xi}(t_n)] + \frac{h}{2} \dot{E}_{nl} [\boldsymbol{\xi}(t_n)] + C_0}} \mathbf{g} \left[\boldsymbol{\xi}(t_n) + \frac{h}{2} \dot{\boldsymbol{\xi}}(t_n) \right] \\ &= \frac{h}{2} (\psi(t_n) + \psi(t_{n+1})) \mathbf{s} \left(\boldsymbol{\xi}(t_n), \dot{\boldsymbol{\xi}}(t_n) \right), \end{aligned} \quad (\text{D.12})$$

where

$$\mathbf{s} \left(\boldsymbol{\xi}(t_n), \dot{\boldsymbol{\xi}}(t_n) \right) : \mathbb{R}^N = \frac{\mathbf{g} \left[\boldsymbol{\xi}(t_n) + \frac{h}{2} \dot{\boldsymbol{\xi}}(t_n) \right]}{\sqrt{2} \sqrt{E_{nl} [\boldsymbol{\xi}(t_n)] + \frac{h}{2} \dot{\boldsymbol{\xi}}(t_n) \cdot \mathbf{g} [\boldsymbol{\xi}(t_n)] + C_0}}. \quad (\text{D.13})$$

Here we encountered the problem of how to approximate the values of \mathbf{g} and E_{nl} at mid step $t_{n+\frac{1}{2}}$. Unlike the several interpolation methods used in [30], we chose a more direct first-order approximation approach using $\dot{E}_{nl}[\boldsymbol{\xi}(t_n)]$ and $\dot{\boldsymbol{\xi}}(t_n)$. $\dot{\mathbf{g}}(\boldsymbol{\xi}(t_n))$ was not used because its expression involving \mathbf{J} may be hard to write, and we instead did a slightly worse approximation using only $\dot{\boldsymbol{\xi}}(t_n)$; it is also viable to approximate $\dot{\mathbf{g}}(\boldsymbol{\xi}(t_n))$ using $\mathbf{g}(\boldsymbol{\xi}(t_{n-1}))$ and $\mathbf{g}(\boldsymbol{\xi}(t_n))$. Notice that in (D.12) $\psi(t_{n+1})$ is unknown, so we need to discretize (D.11) for another update scheme

$$\begin{aligned} \psi(t_{n+1}) - \psi(t_n) &\approx \frac{1}{\sqrt{2}} \frac{(\boldsymbol{\xi}(t_{n+1}) - \boldsymbol{\xi}(t_n)) \cdot \mathbf{g} \left(\boldsymbol{\xi}(t_{n+\frac{1}{2}}) \right)}{\sqrt{E_{nl} [\boldsymbol{\xi}(t_{n+\frac{1}{2}})]}} \\ &\approx (\boldsymbol{\xi}(t_{n+1}) - \boldsymbol{\xi}(t_n)) \cdot \mathbf{s} \left(\boldsymbol{\xi}(t_n), \dot{\boldsymbol{\xi}}(t_n) \right). \end{aligned} \quad (\text{D.14})$$

It now suffices to formulate the whole discretization of nonlinear ODEs as

$$\mathbf{M} \left[\dot{\boldsymbol{\xi}}(t_{n+1}) - \dot{\boldsymbol{\xi}}(t_n) \right] + \mathbf{C} [\boldsymbol{\xi}(t_{n+1}) - \boldsymbol{\xi}(t_n)] + \mathbf{K} \int_{t_n}^{t_{n+1}} \boldsymbol{\xi} dt + \int_{t_n}^{t_{n+1}} \mathbf{g} [\boldsymbol{\xi}] dt = \int_{t_n}^{t_{n+1}} \mathbf{f} dt \quad (\text{D.15})$$

Combining this with SAV and

$$\begin{aligned}\boldsymbol{\xi}(t_{n+1}) - \boldsymbol{\xi}(t_n) &\approx \frac{h}{2} [\dot{\boldsymbol{\xi}}(t_n) + \dot{\boldsymbol{\xi}}(t_{n+1})] \\ \dot{\boldsymbol{\xi}}(t_{n+1}) &\approx \frac{2}{h}\boldsymbol{\xi}(t_{n+1}) - \frac{2}{h}\boldsymbol{\xi}(t_n) - \dot{\boldsymbol{\xi}}(t_n),\end{aligned}\quad (\text{D.16})$$

we obtain the major update scheme:

$$\begin{aligned}\mathbf{M} \left[\frac{2}{h}\boldsymbol{\xi}(t_{n+1}) - \frac{2}{h}\boldsymbol{\xi}(t_n) - 2\dot{\boldsymbol{\xi}}(t_n) \right] + \mathbf{C} [\boldsymbol{\xi}(t_{n+1}) - \boldsymbol{\xi}(t_n)] + \frac{h}{2}\mathbf{K} [\boldsymbol{\xi}(t_n) + \boldsymbol{\xi}(t_{n+1})] \\ + h\psi(t_n)\mathbf{s} + \frac{h}{2}\mathbf{s}\mathbf{s}^\top [\boldsymbol{\xi}(t_{n+1}) - \boldsymbol{\xi}(t_n)] = h\mathbf{f}(t_n) + \frac{h^2}{2}\dot{\mathbf{f}}(t_n)\end{aligned}\quad (\text{D.17})$$

$$\boldsymbol{\xi}(t_{n+1}) = \mathbf{Z}_1^{-1} \left[\mathbf{Z}_0\boldsymbol{\xi}(t_n) + 2\mathbf{M}\dot{\boldsymbol{\xi}}(t_n) + h\mathbf{f}(t_n) + \frac{h^2}{2}\dot{\mathbf{f}}(t_n) \right], \quad (\text{D.18})$$

where

$$\begin{aligned}\mathbf{Z}_0 &= \frac{2}{h}\mathbf{M} + \mathbf{C} - \frac{h}{2}\mathbf{K} + \frac{h}{2}\mathbf{s}\mathbf{s}^\top, \\ \mathbf{Z}_1 &= \frac{2}{h}\mathbf{M} + \mathbf{C} + \frac{h}{2}\mathbf{K} + \frac{h}{2}\mathbf{s}\mathbf{s}^\top.\end{aligned}\quad (\text{D.19})$$

Therefore, the SAV update scheme consists of three steps:

1. Input $\boldsymbol{\xi}(t_n)$, $\dot{\boldsymbol{\xi}}(t_n)$, $\psi(t_n)$ into (D.18) to compute $\boldsymbol{\xi}(t_{n+1})$.
2. Input $\boldsymbol{\xi}(t_n)$, $\dot{\boldsymbol{\xi}}(t_n)$, $\boldsymbol{\xi}(t_{n+1})$ into (D.16) to compute $\dot{\boldsymbol{\xi}}(t_{n+1})$.
3. Input $\boldsymbol{\xi}(t_n)$, $\dot{\boldsymbol{\xi}}(t_n)$, $\boldsymbol{\xi}(t_{n+1})$, $\psi(t_n)$ into (D.14) to compute $\psi(t_{n+1})$.

It can be seen that the major update scheme (D.18) is linear w.r.t. $\boldsymbol{\xi}(t_{n+1})$, allowing for efficient time stepping. However, we notice that $\mathbf{s}\mathbf{s}^\top$ in (D.19) is a fully dense $N \times N$ matrix that may be infeasible to store and solve for large number DOFs. This problem can be well alleviated by performing eigen decomposition only once to the time-invariant matrix

$$\mathbf{Z}_2 = \frac{2}{h}\mathbf{M} + \mathbf{C} + \frac{h}{2}\mathbf{K}, \quad \mathbf{Z}_2^{-1} \approx \boldsymbol{\Phi}\boldsymbol{\Lambda}\boldsymbol{\Phi}^\text{H}, \quad (\text{D.20})$$

where the dimension of $\boldsymbol{\Phi}$ and $\boldsymbol{\Lambda}$ is $M \ll N$, as only the smallest M eigenvalues and corresponding eigenvectors are needed. This should be regarded as a generalized eigenvalue problem because it is desired to avoid explicit matrix inversion. Then by the Shermann–Morrison–Woodbury formula we have

$$\mathbf{Z}_1^{-1} = \left(\mathbf{Z}_2 + \frac{h}{2}\mathbf{s}\mathbf{s}^\top \right)^{-1} = \mathbf{Z}_2^{-1} - \left(\frac{2}{h} + \mathbf{s}^\top \mathbf{Z}_2^{-1} \mathbf{s} \right)^{-1} (\mathbf{Z}_2^{-1} \mathbf{s}) (\mathbf{Z}_2^{-1} \mathbf{s})^\top, \quad (\text{D.21})$$

where \mathbf{Z}_2^{-1} can be approximated by the truncated eigenvalues and eigenvectors. In this way \mathbf{Z}_1^{-1} multiplying a vector can be efficiently computed without storing and inverting a $N \times N$ dense matrix.

To investigate the energy property of this SAV scheme, we multiply $\frac{1}{h}[\boldsymbol{\xi}(t_{n+1}) - \boldsymbol{\xi}(t_n)] = \frac{1}{2}[\dot{\boldsymbol{\xi}}(t_n) + \dot{\boldsymbol{\xi}}(t_{n+1})]$ on both sides of (D.17) to yield¹⁰

$$\begin{aligned}&\frac{1}{2}\dot{\boldsymbol{\xi}}(t_{n+1}) \cdot \mathbf{M}\dot{\boldsymbol{\xi}}(t_{n+1}) - \frac{1}{2}\dot{\boldsymbol{\xi}}(t_n) \cdot \mathbf{M}\dot{\boldsymbol{\xi}}(t_n) + \frac{1}{h} [\boldsymbol{\xi}(t_{n+1}) - \boldsymbol{\xi}(t_n)] \cdot \mathbf{C} [\boldsymbol{\xi}(t_{n+1}) - \boldsymbol{\xi}(t_n)] \\ &+ \frac{1}{2}\boldsymbol{\xi}(t_{n+1}) \cdot \mathbf{K}\boldsymbol{\xi}(t_{n+1}) - \frac{1}{2}\boldsymbol{\xi}(t_n) \cdot \mathbf{K}\boldsymbol{\xi}(t_n) + \frac{1}{2}\psi(t_{n+1})^2 - \frac{1}{2}\psi(t_n)^2 \\ &= [\boldsymbol{\xi}(t_{n+1}) - \boldsymbol{\xi}(t_n)] \cdot \left[\mathbf{f}(t_n) + \frac{h}{2}\dot{\mathbf{f}}(t_n) \right].\end{aligned}\quad (\text{D.22})$$

¹⁰The reason for the equality $\frac{1}{h}[\boldsymbol{\xi}(t_{n+1}) - \boldsymbol{\xi}(t_n)] = \frac{1}{2}[\dot{\boldsymbol{\xi}}(t_n) + \dot{\boldsymbol{\xi}}(t_{n+1})]$ to hold here is that this equation is the actual numerical update scheme we use, no matter how approximate it is to the true continuous values.

Combining this with the definition of E , E_k , E_p , E_{nl} , we obtain the evolution of discrete energy as

$$E[\boldsymbol{\xi}(t_{n+1})] - E[\boldsymbol{\xi}(t_n)] = [\boldsymbol{\xi}(t_{n+1}) - \boldsymbol{\xi}(t_n)] \cdot \left[\mathbf{f}(t_n) + \frac{h}{2} \dot{\mathbf{f}}(t_n) \right] - \frac{1}{h} \|\boldsymbol{\xi}(t_{n+1}) - \boldsymbol{\xi}(t_n)\|_{\mathbf{C}}^2, \quad (\text{D.23})$$

where $\|\mathbf{x}\|_{\mathbf{A}}^2 = \mathbf{x}^\top \mathbf{A} \mathbf{x}$. Since \mathbf{C} is normally positive definite, the discrete energy is guaranteed to dissipate if \mathbf{g} is conservative and energy injection through $\mathbf{f}(t)$ becomes zero. Therefore, it can be concluded that the SAV scheme applied here is energy stable at least for kinetic energy, potential energy, nonlinear ‘‘symmetric’’ energy, and damping.

However, it seems energy stability may fail to satisfy for the non-symmetric forces $\mathbf{f}(t)$, which we should actually write as an operator $\mathbf{f}[\boldsymbol{\xi}(t), \dot{\boldsymbol{\xi}}(t), \ddot{\boldsymbol{\xi}}(t)]$. These non-symmetric ‘‘endogenous’’ forces often relate to the coupling between systems. For example, for the soundboard system, \mathbf{f} is the string’s surface force exerted on the soundboard. If \mathbf{f} is fully linear with respect to the unknowns, then we can use t_{n+1} values in \mathbf{f} to construct linearly implicit schemes which effectively avoids energy instability, though the formulas may be cumbersome to write. But if \mathbf{f} exhibits nonlinearity and t_{n+1} values are used to avoid energy instability, the scheme would become nonlinearly implicit and it seems only implicit methods, e.g. backward differentiation formula (BDF), can solve for the unknown DOFs. We thus conclude that SAV does not address well the non-symmetric forces, which is vital for modeling the nonlinear coupling between the distinct subsystems of the piano. A tradeoff is to keep using energy-unstable linear schemes for the nonlinear non-symmetric forces, but perform several iterations as proposed in section 7.2 to compensate. We hope to see more developments regarding efficient and energy-stable schemes for nonlinear inter-system coupling.

We now consider an example of nonlinear potential energy arising from large deformations. For a 3D elastic solid with large deformations, a major source of nonlinearity is the quadratic term in the Green-Lagrange strain. The tensor and vector versions of this nonlinear strain (linear parts omitted) are

$$\boldsymbol{\epsilon}_{nl}(\mathbf{x}, t) = \frac{1}{2} \sum_{i=1}^3 (\nabla u_i) (\nabla u_i)^\top, \quad (\text{D.24})$$

$$\Rightarrow \vec{\epsilon}_{nl}(\mathbf{x}, t) = \mathcal{A}(\mathbf{u}(\mathbf{x}, t)) = \sum_{i=1}^3 \begin{bmatrix} \frac{1}{2} (\partial_x u_i)^2 \\ \frac{1}{2} (\partial_y u_i)^2 \\ \frac{1}{2} (\partial_z u_i)^2 \\ (\partial_x u_i) (\partial_y u_i) \\ (\partial_x u_i) (\partial_z u_i) \\ (\partial_y u_i) (\partial_z u_i) \end{bmatrix} \quad (\text{D.25})$$

where $\mathcal{A} : \mathbb{R}^3 \rightarrow \mathbb{R}^6$ is a nonlinear operator. From the nonlinear strain, we find the conservative part of nonlinear strain energy functional as

$$E_{nl}[\mathbf{u}(\mathbf{x}, t)] = \frac{1}{2} \int_{\Omega} \mathcal{A}(\mathbf{u}(\mathbf{x}, t)) \cdot \mathbf{D}\mathcal{A}(\mathbf{u}(\mathbf{x}, t)) \, dV. \quad (\text{D.26})$$

Taking gradient of this functional, the nonlinear stress (body force version) is derived as

$$\nabla \cdot \boldsymbol{\sigma}_{nl} = \frac{\delta E_{nl}[\mathbf{u}]}{\delta \mathbf{u}}. \quad (\text{D.27})$$

Besides E_{nl} , there may exist damping proportional to the nonlinear stress, leading to the non-conservative part of nonlinear strain energy functional as

$$E_{nlnc}[\mathbf{u}(\mathbf{x}, t'), t] = \int_0^t \int_{\Omega} \dot{\mathcal{A}}(\mathbf{u}(\mathbf{x}, t')) \cdot 2\mu \mathbf{D}\dot{\mathcal{A}}(\mathbf{u}(\mathbf{x}, t')) \, dV dt', \quad (\text{D.28})$$

where 2μ is the viscous damping coefficient. The dynamics of energy dissipation can then be revealed as

$$\partial_t E_{nlnc}[\mathbf{u}(\mathbf{x}, t'), t] = \int_{\Omega} \dot{\mathcal{A}}(\mathbf{u}(\mathbf{x}, t)) \cdot 2\mu \mathbf{D}\dot{\mathcal{A}}(\mathbf{u}(\mathbf{x}, t)) \, dV. \quad (\text{D.29})$$

However, consideration of nonlinear damping seems lacking in existing IEQ and SAV research. This may stem from that energy dissipation is path-dependent thus the integration over $[0, t]$ can

not be eliminated. This would require some additional but still acceptable computation costs, and has been covered by our nonlinear energy model D.3. In existing research applying IEQ or SAV to musical instruments simulation, there can be no damping [36] or linear damping [16]. Now we apply space discretization to the nonlinear strain energy functional. Based on (2.15) (2.17) we should be able to find

$$\vec{\tau}_{nl}(\mathbf{x}, t) = \mathbf{A}(\mathbf{x}, \boldsymbol{\xi}(t)) + \mathbf{A}_0(\mathbf{x}, \boldsymbol{\xi}(t), \boldsymbol{\xi}_0(t)), \quad (\text{D.30})$$

where \mathbf{A} and \mathbf{A}_0 are $(\mathbb{R}^3, \mathbb{R}^N) \rightarrow \mathbb{R}^6$ and $(\mathbb{R}^3, \mathbb{R}^N, \mathbb{R}^{N_0}) \rightarrow \mathbb{R}^6$ nonlinear functions (a narrower concept than operator) respectively; \mathbf{A} accounts for the conservative part and \mathbf{A}_0 accounts for the non-conservative part when $\boldsymbol{\xi}_0$ is nonzero. For simplicity, the detailed expression of \mathbf{A} and \mathbf{A}_0 are currently not presented here. The nonlinear strain energy functional is then

$$E_{nl}[\boldsymbol{\xi}(t)] = \frac{1}{2} \int_{\Omega} \mathbf{A}(\mathbf{x}, \boldsymbol{\xi}(t)) \cdot \mathbf{D}\mathbf{A}(\mathbf{x}, \boldsymbol{\xi}(t)) \, dV, \quad (\text{D.31})$$

and its variation and first derivative are

$$\begin{aligned} \delta E_{nl}[\boldsymbol{\xi}(t)] &= \delta \boldsymbol{\xi} \cdot \mathbf{B}(\boldsymbol{\xi}(t)), \\ \partial_t E_{nl}[\boldsymbol{\xi}(t)] &= \dot{\boldsymbol{\xi}}(t) \cdot \mathbf{B}(\boldsymbol{\xi}(t)), \\ \mathbf{B}(\boldsymbol{\xi}) &= \int_{\Omega} [\nabla_{\boldsymbol{\xi}} \mathbf{A}(\mathbf{x}, \boldsymbol{\xi})]^\top \mathbf{D}\mathbf{A}(\mathbf{x}, \boldsymbol{\xi}) \, dV \end{aligned} \quad (\text{D.32})$$

Since \mathbf{A}_0 relates to $\boldsymbol{\xi}_0(t)$, i.e. nonzero Dirichlet boundary conditions, it does not satisfy the symmetry (self-adjoint) condition previously highlighted. We thereby seek to compute the nonlinear virtual strain energy as

$$\begin{aligned} \delta E_{nl,0}[\boldsymbol{\xi}(t)] &= \delta \boldsymbol{\xi} \cdot \mathbf{B}_0(\boldsymbol{\xi}(t), \boldsymbol{\xi}_0(t)) \\ \mathbf{B}_0(\boldsymbol{\xi}, \boldsymbol{\xi}_0) &= \int_{\Omega} [\nabla_{\boldsymbol{\xi}} \mathbf{A}(\mathbf{x}, \boldsymbol{\xi})]^\top \mathbf{D}\mathbf{A}_0(\mathbf{x}, \boldsymbol{\xi}, \boldsymbol{\xi}_0) \, dV \\ &\quad + \int_{\Omega} [\nabla_{\boldsymbol{\xi}} \mathbf{A}_0(\mathbf{x}, \boldsymbol{\xi}, \boldsymbol{\xi}_0)]^\top \mathbf{D}[\mathbf{A}(\mathbf{x}, \boldsymbol{\xi}) + \mathbf{A}_0(\mathbf{x}, \boldsymbol{\xi}, \boldsymbol{\xi}_0)] \, dV \end{aligned} \quad (\text{D.33})$$

Finally, we add \mathbf{B} to \mathbf{g} and add $-\mathbf{B}_0$ to \mathbf{f} in the nonlinear ODEs (D.1). Note that since the nonlinear stress belongs to conservative forces, its corresponding nonlinear strain energy functional (D.31) has eliminated the integration over $[0, t]$. This makes it simple to compute the $E_{nl}[\boldsymbol{\xi}(t_n)]$ in (D.13).